ELEMENTA
Science of the Anthropocene

Ranjithkumar, A, et al. 2025. Direct observation of Arctic Sea salt aerosol production from blowing snow and modeling over a changing sea ice environment. *Elem Sci Anth*, 13: 1. DOI: https://doi.org/10.1525/elementa.2024.00006

RESEARCH ARTICLE

Direct observation of Arctic Sea salt aerosol production from blowing snow and modeling over a changing sea ice environment

Ananth Ranjithkumar[1,2,*], Eliza Duncan[2], Xin Yang[1], Daniel G. Partridge[2], Thomas Lachlan-Cope[1], Xianda Gong[3,4], Kouichi Nishimura[5], and Markus M. Frey[1,*]

In the polar regions, there is significant model bias in the number concentrations and seasonality of sea salt aerosol (SSA) due to the lack of understanding of aerosol sources associated with sea ice, which is hampering accurate climate forecasts at high latitudes. Recently, SSA originating from the sublimation of blowing snow has been directly observed to be an important source of aerosol particles in the Antarctic during winter/spring, validating a mechanism proposed a decade ago. Here, we report in situ observations of coarse aerosol production (particle diameter 0.5–20.0 μm) dominated by sea salt from blowing snow above sea ice during winter/spring in the Central Arctic during the MOSAiC (Multidisciplinary drifting Observatory for the Study of Arctic Climate) expedition from October 2019 to September 2020. Blowing snow conditions occurred 20–40% of the time during each of the months from December 2019 to April 2020, with a total of 26 blowing snow events. During blowing snow periods, coarse aerosol number concentrations increased often by an order of magnitude compared to no-blowing snow periods. Mass fractions of sodium chloride in submicron aerosol (particle diameter 0.01–0.625 μm) available during December 2019 and 10 m wind speed showed a significant correlation ($R = 0.61$, $P < 0.05$), indicating that much of the aerosol observed during storms is sea salt released by sublimating blowing snow. We use these observations to refine the current model parameterization by considering the spatial and temporal variability of atmospheric and sea ice conditions. Snow particle size distributions and snow salinities are expressed as a function of wind speed and snowpack depth, respectively, which can be easily implemented into climate models. Validation of the snow particle size distribution parameterization with previous polar winter observations showed agreement in the Arctic (N-ICE2015 cruise, March 2015) above the threshold for drift and blowing snow, but a negative bias in the Antarctic (Weddell Sea, June to August 2013). Updating the blowing snow mechanism in the chemical transport model p-TOMCAT with wind-dependent snow particle size distributions results in 14% more SSA produced and a slightly better correlation with MOSAiC observations of coarse aerosol ($R = 0.28$). Significant increases in aerosol number concentration due to blowing snow sublimation are calculated by as much as 70 cm^{-3} during the Antarctic winter and 50 cm^{-3} during the Arctic winter compared to a baseline simulation with no blowing snow. Thus, taking into account SSA from blowing snow above sea ice will be important to improve model predictions of polar aerosol and climate.

Keywords: Blowing snow, Aerosol, Sea salt, MOSAiC, Arctic

[1] British Antarctic Survey, Natural Environment Research Council, Cambridge, UK

[2] Department of Mathematics and Statistics, Faculty of Environment, Science and Economy, University of Exeter, Exeter, UK

[3] Research Center for Industries of the Future, Westlake University, Hangzhou, Zhejiang, China

[4] Key Laboratory of Coastal Environment and Resources of Zhejiang Province, School of Engineering, Westlake University, Hangzhou, Zhejiang, China

[5] Graduate School of Environmental Studies, Nagoya University, Nagoya, Japan

*Corresponding authors:
Emails: A.R.Ranjithkumar@exeter.ac.uk; maey@bas.ac.uk

1. Introduction

The Arctic climate system in polar regions has been changing rapidly as a consequence of anthropogenic activity (Overland et al., 2019), with some studies showing surface temperatures increasing at 4 times the global average rate (Rantanen et al., 2022). Aerosol particles are an integral part of the climate system and the polar regions are particularly sensitive to changes in aerosol concentrations (Carslaw et al., 2013; Pithan and Mauritsen, 2014). Aerosol particles can affect the global energy balance by directly absorbing or scattering solar radiation and indirectly by their ability to act as cloud condensation nuclei (CCN) and as ice nucleating particles (INP) and thereby

impact cloud microphysics (Twomey, 1977; Albrecht, 1989). In the assessment of anthropogenic forcing, radiative effects of aerosols have been identified as the largest source of uncertainty in climate forecasts (Bellouin et al., 2020).

Primary sea salt aerosol (SSA) emissions over most of the earth originate from wave breaking and bubble bursting close to the ocean surface (de Leeuw et al., 2011) and can scatter solar radiation and influence cloud properties (O'Dowd et al., 1997; Quinn et al., 2002). In addition, SSA is a large reservoir of various chemical compounds, such as reactive halogens, particularly bromine (Fan and Jacob, 1992; Sander et al., 2003), which, after release, drive springtime ozone and mercury depletion events in the Arctic (Gao et al., 2022) and thus influence the oxidizing capacity of the atmosphere (Yang et al., 2005; Yang et al., 2020; Marelle et al., 2021). SSA is also used as an ice core proxy for past sea ice conditions (Abram et al., 2013; Levine et al., 2014) since there is strong evidence that sea ice is a significant source of SSA. SSA concentration maxima are observed in the polar atmosphere during winter, for example, in coastal Antarctica (Rankin and Wolff, 2003), East Antarctic Plateau (Legrand et al., 2016), and Arctic (e.g., Rhodes et al., 2017), and ice core records from the polar ice sheets show a factor of 2.5–4 increase in the SSA deposition flux during glacial periods in comparison to warmer interglacial periods (Wolff et al., 2003; Abram et al., 2013), indicating SSA supply is highest when the sea ice is at its seasonal or long-term maximum. Another point of evidence for sea ice source of SSA is that tropospheric SSA over the Antarctic coast is strongly depleted in sulfate (SO_4^{2-}) with respect to sodium (Na^+) in comparison to seawater (Wagenbach et al., 1998), so are frost flowers in the sea ice zone (Rankin et al., 2000) and snow on sea ice (Frey, et al., 2020). When sea ice brine cools down to its eutectic point, precipitation of mirabilite ($Na_2SO_4\ 10H_2O$) starts to occur at temperatures less than $-6.4°C$, and SO_4^{2-} is removed from the liquid phase to a larger extent than Na^+, resulting in fractionation leading to liquid and solid phase SO_4^{2-}:Na^+ ratios that are dissimilar to bulk seawater (Frey et al., 2020). Additionally, in the polar regions, hydrohalite ($NaCl{\cdot}2H_2O$) can also precipitate at colder conditions (approximately $-23°C$) (Hara et al., 2012; Hara et al., 2017), further altering the chemical composition of the remaining brine relative to seawater. Frost flowers, which are highly saline, also exhibit a similar sulfur depletion (Rankin et al., 2000), but past studies have shown that frost flowers are not easily airborne and do not occur widely enough to produce large enough concentrations of SSA (Roscoe et al., 2011; Hara et al., 2017; Yang et al., 2017). A hypothesis that the sublimation of saline blowing snow could be the source of this SSA (Yang et al., 2008) has recently been validated by observations from the Weddell Sea during the Antarctic winter (Frey et al., 2020), and its microphysical mechanism is supported by laboratory studies (Závacká et al., 2022; Vetráková et al., 2023).

Most CMIP6 climate models include only SSA originating from the open ocean and do not reproduce the observed winter maxima of SSA concentration in the Antarctic and Arctic (Huang and Jaeglé, 2017; Rhodes et al., 2017; Yang et al., 2019; Lapere et al., 2023) due to the lack of representation of wintertime sources of SSA over sea ice. SSA can scatter solar radiation and act as CCN (Clarke et al., 2006) and as INP (DeMott et al., 2016; Wagner et al., 2018). Therefore, it is critical to accurately quantify SSA in polar regions, to better estimate its impact on the radiation balance, tropospheric halogen chemistry and on inferring past sea ice extent from polar ice cores. Sea ice sources of SSA include open leads (Chen et al., 2022), frost flowers (Rankin et al., 2000), and salty blowing snow undergoing sublimation (Yang et al., 2019), where the latter has been found to dominate in Antarctic winter/spring (Frey et al., 2020). Open leads will play an increasingly larger role in a changing sea ice environment, whereas frost flowers are less likely to get airborne and therefore only play a minor role (Roscoe et al., 2011; Huang and Jaeglé, 2017). The blowing snow SSA production mechanism, where saline snow particles on the sea ice are lofted into the atmosphere by turbulent winds followed by sublimation and release of SSA, has been implemented to date in the chemistry transport models GEOS-Chem (Huang and Jaeglé, 2017; Gong et al., 2023), p-TOMCAT (Legrand et al., 2016; Rhodes et al., 2017; Yang et al., 2019), and WRF-Chem (Marelle et al., 2021) to investigate the impact of this newly identified SSA source on high latitude near-surface sodium in aerosol and tropospheric halogen chemistry. Implementation of the blowing snow atmospheric process (Yang et al., 2008) into these models improved the SSA comparison with observations, and the models were able to better simulate the temporal and geographic variability of SSA concentration, including the winter maximum at both Poles (Levine et al., 2014; Huang and Jaeglé, 2017).

The snow particle size distribution and snow salinity are important factors that influence the SSA production mass flux (Q_{SSA}) from blowing snow (Yang et al., 2008). The parameterization for the blowing snow mechanism in a recent study using p-TOMCAT applies a fixed blowing snow particle size distribution and snow salinity and does not consider their temporal and spatial variability, and thereby cannot resolve individual storms or different snowpacks on first-year and multi-year sea ice (Yang et al., 2019). The salinity of snow on sea ice in polar regions is determined by several possible processes: (1) the upward migration of brine from the sea ice surface into the snowpack, driven by capillary action, (2) heavy snow loading causing flooding of the ice floe and delivering seawater to the bottom of the snowpack, (3) highly saline frost flowers contaminating the snow, and (4) atmospheric deposition of SSA advected from the open ocean or nearby sea ice sources (open leads, blowing snow, frost flowers). The blowing snow model mechanism is subject to uncertainties due to limited observations of salinity and snow particle distribution.

In this study, we report first observations in the Central Arctic of coarse SSA produced by blowing snow during the year-round MOSAiC (Multidisciplinary drifting Observatory for the Study of Arctic Climate) 2019–2020 expedition. We perform a sensitivity analysis to identify the most sensitive parameters of the blowing snow parameterization. We use

comprehensive measurements of the relevant parameters undertaken during the MOSAiC 2019–2020 expedition to improve the most recent model parameterization (Yang et al., 2019). In climate models, the SSA from the open ocean is parameterized as a function of the 10-m wind speed (Monahan et al., 1983; Gong, 2003), therefore, to maintain consistency, in this work we characterize Q_{SSA} from sea ice also as a function of the 10 m wind speed. This new parameterization has been used in a recent study (Gong et al., 2023) and the SSA from blowing snow is shown to contribute to a surface warming of up to $+2.3$ W m^{-2} under cloudy sky conditions in the Arctic winter. In this study, we document the development and validation of this parameterization against previous measurements in the Arctic (N-ICE 2015) (Graham et al., 2017; Frey et al., 2019) and Antarctic (Weddell Sea) (Frey et al., 2020) using the chemistry transport model p-TOMCAT.

2. Methods

2.1. Mechanism for sea salt production from blowing snow

Past work (Yang et al., 2019) explores 2 potential mechanisms for the formation of SSA from blowing snow, where the evaporation rate is controlled by either the Kelvin effect or the moisture gradient. In mechanism 1, the sublimation rate is controlled by the Kelvin effect where the curvature of the snow crystals drives the initial stages of the sublimation process under saturated conditions (Jambon-Puillet et al., 2018). Mechanism 2 assumes that the moisture gradient between the snow particles and ambient air controls the water loss rate and therefore must occur in a subsaturated layer (Cascajo-Castresana et al., 2021). However, for mechanism 2 to produce results that agree with observations, it is necessary to assume that multiple SSAs are formed from a single blown snow particle, and in mechanism 1, this assumption is not necessary. From a past study (Yang et al., 2019), both mechanisms produce results comparable to observed aerosol concentrations for particles whose diameter is larger than 0.4 μm but deviates significantly for particles smaller than 0.4 μm. We consider only mechanism 1 in this study. We use the measurements from MOSAiC described in the next section to improve the current model representation.

2.2. Measurements

The main dataset used in this study is from the MOSAiC expedition, which is, to date, the most extensive measurement campaign in the Central Arctic (Shupe et al., 2022). This is a year-long dataset that was collected as the German research vessel (RV) *Polarstern* drifted in the Arctic Sea ice. **Figure 1** shows the MOSAiC ship drift track, starting in October 2019 from 85°N, 136°E when the ship was moored to a suitable ice floe (Krumpen et al., 2020). For most of the expedition, the ship passively drifted in the sea ice beside the ice floe, with a few exceptions which included a short cruise between mid-May and mid-June 2020 to Svalbard (Norway) for crew exchange and a cruise to relocate the ship back into the pack ice further north in July 2020, after the ice floe led the ship into the marginal sea ice zone. The instruments onboard the ship were operational during both the passive drift phase and transit phase of the expedition, except between June 3 and June 8 when the ship was in the territorial waters of Svalbard. The expedition ended in September 2020, and most of the measurements were obtained in the central Arctic Ocean North of 80°N, within the pack ice. **Table 1** summarizes the observed parameters used in this study, including instruments, data resolution and uncertainty, and location where the measurements were collected during MOSAiC.

Other measurements used in this study include observations from previous sea ice expeditions during winter and spring in the Arctic (N-ICE 2015, Frey et al., 2019; Graham et al., 2019) and the Weddell Sea in the Antarctic (Frey et al., 2020). The N-ICE2015 data were obtained from instruments onboard the Norwegian RV *Lance*. The ship was frozen into an ice pack north of Svalbard at 83°N, 22°E and allowed to drift with the ice from January to June 2015 (Granskog et al., 2016). The Weddell Sea measurements were collected during 2 consecutive Antarctic expeditions onboard RV *Polarstern* in 2013. One expedition in winter between June 8 and August 12, 2013, and another expedition in spring between August 14 and October 16, 2013 (Frey et al., 2020).

Airborne snow particles were measured using an open path snow particle counter (SPC-95, Niigata Electric Co., Ltd) (Nishimura et al., 2014; Frey et al., 2020) mounted on the NOAA tower located at the Met City site (**Table 1**), which was located between 300 and 600 m away from the ship during the campaign (Shupe et al., 2022; Cox et al., 2023). The SPC is a single-slit sensor with a laser diode, which measures the number and size of snow particles. The SPC near the surface was mounted within the saltation layer, a layer just above the snow surface usually several centimeters thick, at a mean height of 0.08 m above the snow surface and reset whenever snow accumulation or erosion was observed. The sampling area of the SPC is maintained perpendicular to the wind direction, by mounting it on a self-steering wind vane. Its sampling area A has dimensions (2×10^{-3}) m $\times$ (25×10^{-3}) m and its volume is (2×10^{-3}) m $\times$ (25×10^{-3}) m $\times$ (0.5×10^{-3}) m (Frey et al., 2020). Snow particles passing through the sampling area cause electric pulse signals, which are sent to a transducer and a data logging system. The detected particles are then classified into 1 of 64 mean particle diameter classes ranging from 36 μm to 490 μm. Measurement signals for the smallest diameter class (d_p = 36 μm) have large uncertainties due to the instrument's detection limit, and the signal for the largest diameter class (d_p = 490 μm) displayed frequent spikes due to the detection of large precipitating snow particles (Frey et al., 2020). Therefore, measurements from these two size classes were not used. Particle counts at a sampling rate of 1 Hz are integrated into 1 min values and divided by the sampling area to obtain the particle number flux F (m^{-2} min^{-1}). The meteorological parameters wind speed (U) from a sonic anemometer, temperature (T), and relative humidity (RH) were also measured on the NOAA tower located at the Met City (**Table 1**) (Cox et al., 2023). Using F and the 2-m horizontal wind speed $U_{2\ m}$ extrapolated to

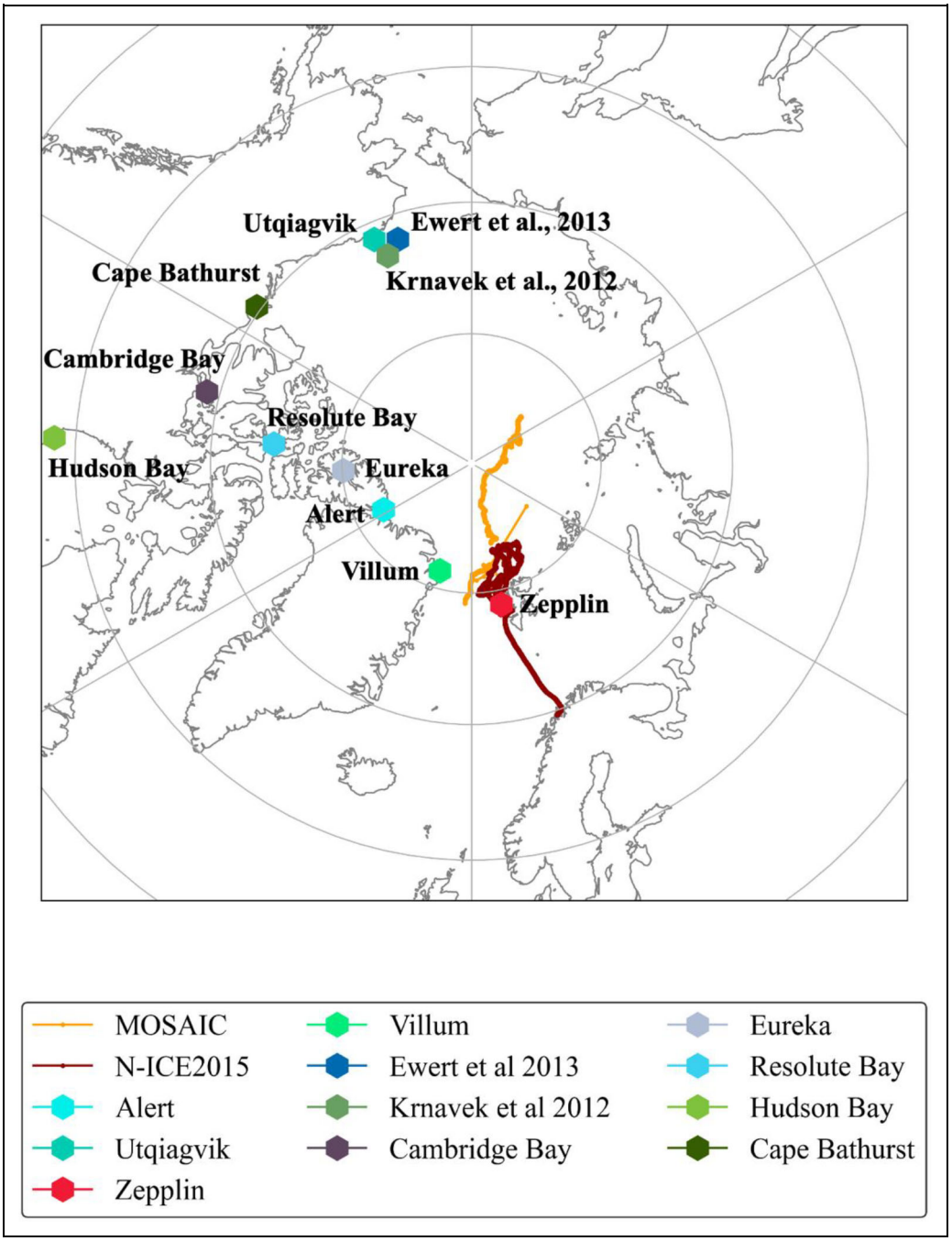

Figure 1. Spatial map of the measurement locations in the Arctic used in this study.

0.1 m assuming a logarithmic wind profile, we compute the snow particle number density $N_{46–478\ \mu m} = F/U$.

A Compact Lightweight Aerosol Spectrometer Probe (CLASP) was used to collect size resolved aerosol number concentration measurements at 2 m above the sea ice mounted on the NOAA tower at the Met City site (**Table 1**). The CLASP is a closed path optical spectrometer that aspirates sample air at a flow rate of 3 L/min (Hill et al., 2008; Norris et al., 2008). Any variability that occurs is controlled and recorded using the onboard electronics, so it can be used to make corrections to the measurements. This original instrument was improved upon (Norris et al., 2008; 2012) and deployed during this expedition. It measures a 16-channel spectrum of aerosol sizes ranging from 0.5 μm to 20 μm at ambient humidity at a sampling rate of 10 Hz and then aggregated to 1-min averages. The instrument was calibrated before and after the expedition. Particle losses in the walls of the inlet were minimized using a straight, short tube of 0.3 m in length (Hill et al., 2008; Norris et al., 2008). We apply a power law pollution filter to the aerosol number concentrations N as described in Beck et al. (2022) to remove any pollution-influenced data ($\sim$0.5% of the data, from December 2019 to May 2020). The method filters the data based on the derivative of the aerosol concentration, where higher derivatives represent periods of contamination with high concentration variability. The raw data from the CLASP are not significantly affected by pollution, with aerosol number concentration

Table 1. Overview of observed parameters, instrument details, and uncertainties during MOSAiC (from October 2019 to September 2020) and used in this study[a]

Parameter	Instrument	Sampling Rate	Uncertainty	Reference
Snow particle number concentration, $N_{46–478}$ (d_p 46–478 µm, 64 size bins) (cm^{-3})	Snow particle counter (SPC-95, Niigata Electric Co., Ltd) at 0.08 m and 10.0 m above the snow surface	1 Hz	~1% in number concentration	Nishimura and Nemoto (2005); Nishimura et al. (2014); Frey et al. (2020)
Aerosol number concentration, $N_{0.5–20}$ (d_p 0.5–20 µm, 16 size bins) (cm^{-3})	Compact Lightweight Aerosol Spectrometer Probe (CLASP) at 2.0 m above the snow surface	10 Hz	1% in number concentration; 10% in size bin width	Hill et al. (2008); Norris et al. (2012)
Mass concentration of aerosol chemical species, $M_{10–625\ nm}$ (d_p 10–625 nm) ($\mu g\ m^{-3}$)[b]	Aerosol Chemical Speciation Monitor (ACSM) at 12.0 m above the snow surface	2 h^{-1}	Limit of detection (LOD) <0.2 $\mu g\ m^{-3}$	Ng et al. (2011)
Snow salinity, S_p (psu)	Salinity, Conductivity, and Temperature sensor (YSI 30, YSI)	1–2 times per week	0.001–0.01 psu (below 1.00 psu)	Macfarlane et al. (2022); Macfarlane et al. (2023); Frey et al. (2020)
Wind speed, U ($m\ s^{-1}$)	Sonic anemometer (USA-1, METEK) at 2.0, 6.0, and 10.0 m above the snow surface	10 Hz	0.3 $m\ s^{-1}$	Cox et al. (2023)
Temperature, T (°C)	PT1000 resistance thermometer (WXT530, VAISALA) at 2.0, 6.0, and 10.0 m above the snow surface	1 Hz	0.3°C	Cox et al. (2023)
Relative humidity, RH (%)	Capacitive HUMICAP R2 sensor (WXT530, VAISALA) at 2.0, 6.0, and 10.0 m above the snow surface	1 Hz	5% (at 90–100%)	Cox et al. (2023)

[a]The snow particle counter, aerosol spectrometer, and meteorology sensors were mounted on the NOAA tower located at Met City between 300 and 600 m away from RV *Polarstern* during the campaign (Shupe et al., 2022), and their measurements are reported at 1-min resolution. The ACSM was located in the ARM container onboard RV *Polarstern*, and snow pits were sampled at various locations on the MOSAiC ice floe to determine snow salinity. Data coverage of each parameter throughout the year is reported in Shupe et al. (2022).

[b]Mass concentrations of non-refractory sub-micron aerosol species, including organics, sulfate, nitrate, and ammonium.

maxima only as high as 130 cm^{-3}, whereas pollution events reported in the Arctic typically have aerosol concentrations greater than 10^4 cm^{-3} (Beck et al., 2022).

Snow pit vertical profiles were sampled at least once per week at various locations on the MOSAiC ice floe, and snow salinity S_p was determined using a Salinity, Conductivity, and Temperature sensor (YSI 30, YSI) (Macfarlane et al., 2023; **Table 1**). Conductivity values were recorded and converted into S_p using the Gibbs Seawater (GSW) Oceanographic Toolbox (McDougall and Barker, 2011), which applies the algorithm of the Practical Salinity Scale of 1978 (PSS-78) with an extension to salinities less than 2 psu (Hill et al., 1986). We also used salinity measurements reported in Confer et al. (2023), which spans a time period from 2004 to 2017. This dataset included measurements on first-year ice at Utqiagvik (71.3°N, 156.6°W) from February 2010 to March 2011 (Ewert et al., 2013). Krnavek et al. (2012) and Peterson et al. (2019) also collected snow samples over first-year sea ice in the Arctic Ocean between 70.2°N, 169.8°W and 89.99°N, 179.65°E during March–April 2004, 2005, 2007, April–May 2013, February 2014, and April 2014. The salinity measurements we used from previous studies were taken over first-year sea ice. However, due to insufficient information to classify all data from the MOSAiC dataset into first-year and multi-year sea ice, we combined all data without distinguishing between ice types.

To characterize aerosol particle chemical composition for sub-micron aerosol particles, the Aerosol Chemical Speciation Monitor (ACSM) (Ng et al., 2011) in the ARM container at the bow of RV *Polarstern* was used to quantify the concentrations of sulfate, nitrate, ammonium, and organic compounds (**Table 1**). A pollution filter was used to flag pollution-affected data similar to the approach by Gong et al. (2023) and Beck et al. (2022). It is important to note that ACSM measurements remain unaffected by pollutants like black carbon, which the ACSM does not detect. As SSA is refractory and cannot be reliably quantified by the ACSM, the total mass concentration of sea salt in the size range of

10–625 nm ($M_{10–625\ nm}$) was derived as described in Gong et al. (2023). In brief, we used the particle size distributions to derive the particle volume size distribution, which in turn allows us to estimate the total particle volume. In these calculations, we assumed a uniform shape factor of 1 and a particle density of 1.6 g cm^{-3} to compute the total particle mass. The mass of sea salt is then determined by subtracting the mass of sulfate, ammonium, nitrate, and organics measured by the ACSM from the total particle mass. These data are only available for a limited period between December 3, 2019, and December 12, 2019. Note that the ACSM measures sub-micron aerosol in the size range of 10–625 nm, so it only partially overlaps with the size range of the CLASP instrument (0.5–20 μm).

2.3. Parameterization of SSA mass flux from blowing snow and sensitivity analysis

The model framework described in Yang et al. (2008; 2019) computes mass flux of SSA from sublimating blowing snow Q_{SSA} in units of kilograms per square meter per second (kg m^{-2} s^{-1}) as:

$$Q_{SSA} = \frac{Q_s}{1000}\int_0^\infty\int_0^\infty f(d_p)S_p\psi(S_p)d(d_p)d(S_p), \quad (1)$$

where Q_s is the bulk sublimation flux of suspended snow particles in units of kilograms per square meter per second (kg m^{-2} s^{-1}), d_p is the snow particle diameter, $f(d_p)$ is the snow particle size distribution, S_p is the snow salinity in practical salinity units (psu), approximately equivalent to the weight of dissolved inorganic matter in grams per kilogram of seawater, and $\psi(S_p)$ is the snow salinity probability distribution. Note that from Equation 1 we can also directly derive particle number flux in units of particles per square meter per second (m^{-2} s^{-1}). The bulk sublimation flux Q_s is derived following the approach described previously by integrating the local bulk sublimation rate over the entire blowing snow column (Rogers and Yau, 1989; Déry and Yau, 1999; 2001) and modified to include the impact of snow age (Yang et al., 2008):

$$Q_s = kA'Q_s'\frac{q_{bsalt}}{q_{b0}}, \quad (2)$$

where A' is an empirical snow age factor (Box et al., 2004). Q_s' is a normalized column integrated sublimation rate in units of millimeter per day (mm d^{-1}) (Rogers and Yau, 1989), k (=1.1574 × 10^{-5}) is a factor to convert Q_s into units of kg m^{-2} s^{-1}. q_{b0} is the blowing snow mixing ratio at the threshold 10-m wind speed, and q_{bsalt} is the blowing snow mixing ratio (kg/kg) in the saltation layer under ambient conditions computed as:

$$q_{bsalt} = 0.385\left(1 - \frac{U_{t,10\,m}}{U_{10\,m}}\right)^{2.59}u_*^{-1}, \quad (3)$$

where u_* is the friction velocity, $U_{10\ m}$ is the 10-m wind speed (m s^{-1}), and $U_{t,10\,m}$ is the threshold wind speed. An empirical expression for $U_{t,10\ m}$ under dry snow conditions was previously derived based on observations from the Canadian prairies as a function of ambient temperature T_a, and the minimum threshold wind speed U_{t0} (=6.9 m s^{-1}), below which no snow drift occurs (Li and Pomeroy, 1997):

$$U_{t,10\,m} = U_{t0} + 0.0033(T_a + 27.27)^2. \quad (4)$$

The snow particle size distribution $f(d_p)$ is approximated by a two-parameter gamma probability density function (PDF) (Budd et al., 1966) with shape and scale parameter α and β, which are related to mean particle diameter d_p (=αβ):

$$f(d_p) = \frac{e^{-\frac{d_p}{\beta}}d_p^{\alpha-1}}{\beta^\alpha\Gamma(\alpha)}. \quad (5)$$

Previous modeling experiments demonstrated that SSA production flux is sensitive to α (Yang et al. (2019). α describes PDF skewness with low values indicating asymmetric distributions with long tails from contribution of larger snow particles observed near the surface and higher values indicating more symmetric distributions higher up in the atmosphere (e.g., Nishimura and Nemoto, 2005). Snow age is also an important parameter that controls how easily snow particles can be uplifted into the atmosphere. Aged snow is thought to be more resistant to wind mobilization (Li and Pomeroy, 1997) and requires a higher threshold wind speed. Other important parameters are roughness length (*RL*) influencing $U_{t,10\ m}$, RH_{ice} impacting snow particle sublimation flux, and snow salinity probability distribution $\psi(S_p)$ controlling SSA mass flux from blowing snow (Equation 1). The sensitivity of Q_{SSA} to $\psi(S_p)$ is explored below by shifting the mean value of $\psi(S_p)$ but keeping the standard deviation constant.

We used Sobol's algorithm for global variance sensitivity to rank the model parameters based on the sensitivity of the calculated SSA number flux from sublimating blowing snow. SSA number rather than mass flux is considered here due to its importance for climate (e.g., Gong et al., 2023) and is related to the SSA mass flux Q_{SSA} in Equation 1 by particle density and volume. Sobol's algorithm allows for the perturbation of all parameters of interest over the parameter space, decomposing the variance of model output into total variances for the input parameters. We estimate the first order and total Sobol's indices (Saltelli et al., 2010), where the first order Sobol Index, S_i, for a parameter i determines the contribution to the output variance of a single parameter (i) as:

$$S_i = \frac{\mathrm{Var}(E[\varphi|\Theta_i])}{\mathrm{Var}(\varphi)}, \quad (6)$$

where φ is the model output and $E[\varphi|\Theta_i]$ is the expectation of the output conditional on the parameter i. However, the total Sobol Index $S_{T,\,i}$ also accounts for the interactions with other input parameters and is calculated as:

$$S_{T,\,i} = \frac{\mathrm{Var}(\varphi) - \mathrm{Var}(E[\varphi|\Theta_{\forall\,j\neq i}])}{\mathrm{Var}(\varphi)}, \quad (7)$$

where $E[\varphi|\Theta_{\forall\,j\neq i}]$ is the expectation of the output conditional on variation of all parameters excluding Θ_i.

Latin hypercube sampling was used to generate a quasi-random sample of parameter values distributed evenly over a sample space: partitioning the cumulative density function for each parameter into evenly spaced

Table 2. List of parameters and their ranges used in the sensitivity analysis

Parameter	Minimum	Maximum
Shape parameter, α	2	11
Temperature, T (°C)	−30	0
Relative humidity, RH (%)	60	100
Wind speed, $U_{10\ m}$ (m s^{-1})	6.9 (=U_{t0})	25
Roughness length, RL (m)	1e−5	1e−2
Mean salinity, S_p (psu)	0.1	10
Snow age, A' (days)	0	30

regions and selecting a random sample from each sample space to obtain random values across the full multidimensional sample space. The total number of samples utilized is determined by the formula $N_{samples} = 1000 * (k + 2)$, where "$k$" represents the seven input parameters, resulting in 9,000 samples. The range of the parameters used for this global sensitivity study is shown in **Table 2**. These parameter ranges were chosen to account for the variability encountered in the lower atmosphere in polar regions based on past studies (King and Anderson, 1994; Andreas et al., 2010; Yang et al., 2019; Frey et al., 2020; Wagner et al., 2022; Confer et al., 2023).

2.4. Model setup

In this study, we use the chemical transport model p-TOMCAT as detailed in Yang et al. (2019), which includes a sea spray emission scheme at high latitude that accounts for the influence of sea surface temperature on SSA production (Jaeglé et al., 2011) and the snow salinity distribution from the MOSAiC measurements (mean S_p = 0.19 psu and standard deviation = 8.7 psu) (Macfarlane et al., 2023). SSAs from sea ice and open ocean are represented in 21 size bins ranging from 0.02 μm to 12 μm. The European Centre for Medium-Range Weather Forecasts (ECMWF) produces 6 hourly reanalysis files for the weather known as the ERA-interim reanalysis meteorological data and realistic model precipitation fields (Legrand et al., 2016), which are read into the model. The relative humidity is also taken from the ERA-interim data. The Hadley Centre Sea Ice and Sea Surface Temperature dataset (Rayner et al., 2003) provided the monthly sea surface temperatures and sea ice coverage for the model. In addition, to allow for maximum sea salt production rate, the parameter of snow age is set to zero days (Yang et al., 2019). The model has 31 vertical levels from the surface up to ∼10 hPa, with a horizontal resolution of 2.8° × 2.8°. The p-TOMCAT model spin-up time of >1 year is used to allow for equilibrium to be established.

We conduct the following simulations:

1. "OO": baseline simulation, where the only source of sea salt in the model is from the open ocean (Jaeglé et al., 2011).
2. "SI – Old Scheme": baseline simulation + SSA from blowing snow based on the existing parameterization with a fixed shape parameter (α = 2) for the snow particle size distribution used in a recent study (Yang et al., 2019).
3. "SI-New Scheme": baseline simulation + SSA from blowing snow based on the new parameterization developed in this study.

We use these simulations to show the impact of the blowing snow on the seasonal mean and seasonal cycle of the aerosol number concentration and sodium mass concentration in polar regions (Section 3.4).

3. Results and discussion

3.1. Observations of snow particles and SSA from blowing snow during MOSAiC

Here, we report snow particle number concentrations $N_{46–478\ \mu m}$ at 10 m from October 15, 2019, to December 1, 2019, and near the surface (∼0.08 m) from December 2, 2019, to May 9, 2020, as well as coarse aerosol number concentration $N_{0.5–20\ \mu m}$ at 2 m above the sea ice. We also included measurements of fine aerosol number concentration (d_p 10–300 nm) and aerosol chemical composition (for d_p < 625 nm) in December 2019 described previously (Gong et al., 2023). The statistics of the entire dataset including $U_{10\ m}$ (**Figure 2**) is summarized in **Table 3**.

During MOSAiC, sub- and super-micron aerosol particles were detected over the Arctic Sea ice during blowing snow events. Our analysis focuses on the December 2, 2019, to May 9, 2020 (159 days) period, when all three parameters ($N_{46–478\ \mu m}$ near the surface 0.08 m, $N_{0.5–20\ \mu m}$ at 2.0 m. and $U_{10\ m}$, are available. We defined blowing snow events as periods lasting over 10 h when both the 10-m wind speed was above the threshold wind speed predicted by Equation 4 ($U_{10\ m} > U_{t,10\ m}$) and snow particles were detected by the SPC near the surface. There were 26 blowing snow events between December 2, 2019, to May 9, 2020 (**Figure 2**; Figures S1–S16 and Table S1). During June and July (data not shown), however, no blowing snow was observed because warmer summertime temperatures (mean $T_{2\ m}$ 0.1°C) increased the threshold wind speed U_t (mean 9.5 m s^{-1}), and were often above 0°C, leading to melt and reduced availability of mobile snow. During the October–November 2019 period, 7 blowing snow events were identified based on the SPC measurements at 10 m (Table S2), which are not included in the development of the parameterization described below. The probability density distribution of $U_{10\ m}$ during MOSAiC shows that approximately 30% of the time (∼47 days between December 1, 2019, and May 9, 2020) $U_{10\ m}$ exceeds the minimum drift threshold wind speed of ∼6.9 m s^{-1} (**Figure 3a**; Equation 4) when snow particles at higher concentrations are detected by the SPC (**Figure 3b**). Note that U_t estimated with Equation 4 is a simple function of air temperature, varied between 6.9 m s^{-1} and 9.9 m s^{-1} during the entire period. Snow physical properties are more complex, and U_t may depend on more factors such as snow age or salinity. Aerosol particles in the size range from 0.5 μm to 20 μm

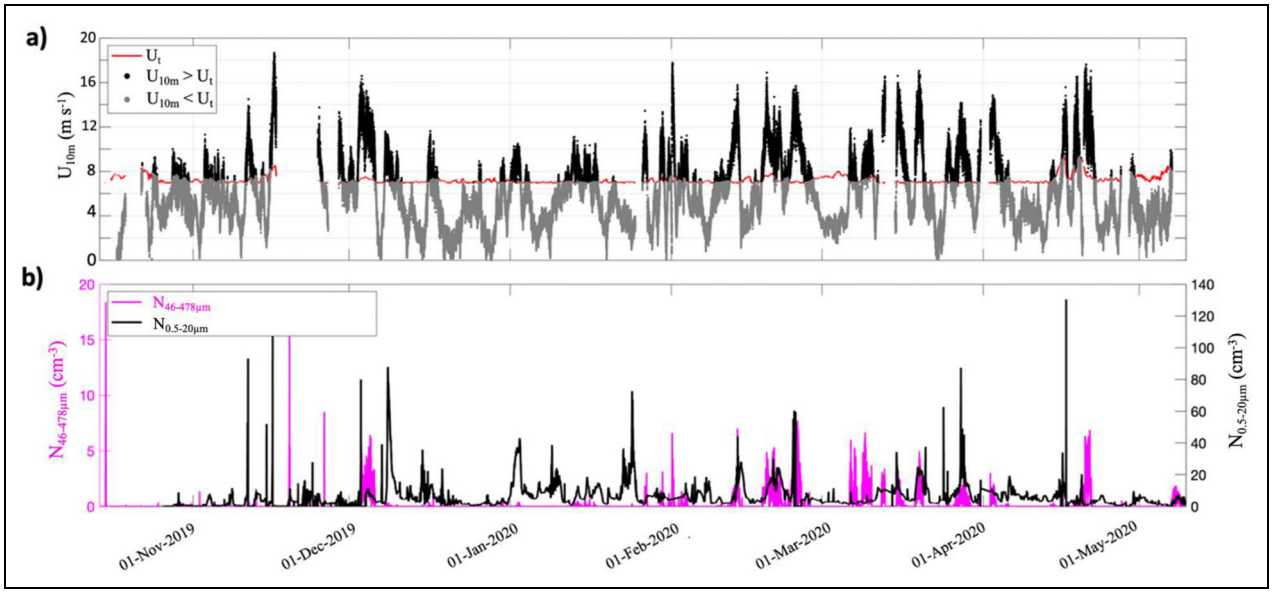

Figure 2. MOSAiC observations from October 2019 to May 2020. (a) 10-meter wind speed ($U_{10\ m}$) and threshold wind speed for blowing snow ($U_{t,10\ m}$), with $U_{10\ m}$ in black symbols when $U_{10\ m} > U_{t,10\ m}$ and in gray symbols when $U_{10\ m} < U_{t,10\ m}$; (b) total snow particle number concentration $N_{46–478\ \mu m}$ (d_p 46–478 µm) near the surface (~0.08 m) and total aerosol number concentration $N_{0.5–20\ \mu m}$ (d_p 0.5–20 µm) at 2 m.

Table 3. A statistical overview of measurements during MOSAiC for the period from December 2, 2019, to May 9, 2020, including snow particles at about 0.08 m and coarse aerosol at 2 m above the snow surface, snow salinity, mass fraction of sea salt in sub-micron aerosol, and wind speed (see also Table 1)

Parameter	Median	Interquartile Range 25th–75th Percentile	Time Period
Snow particle number density, $N_{46–478\ \mu m}$ (d_p 46–478 µm) (cm^{-3})	1.9×10^{-4}	0–7.7×10^{-3}	December 2, 2019, to May 9, 2020 (159 days)
Aerosol number density, $N_{0.5–20\ \mu m}$ (d_p 0.5–20 µm) (cm^{-3})	1.8	1.0–3.1	October 15, 2019, to May 9, 2020 (207 days)
Snow Salinity, S_p (psu)[a]	0.3	0.1–3.0	October 15, 2019, to May 9, 2020
Mass fraction of sea salt in sub-micron aerosol particles (d_p 10–625 nm) (%)[b]	52.2	26.1–67.0	December 2, 2019, to December 10, 2019 (10 days)
Wind speed, $U_{10\ m}$ (m s^{-1})	5.5	3.7–8.1	October 15, 2019, to May 9, 2020 (207 days)

[a]Snow salinity measurements during MOSAiC were collected bi-weekly from snow pits of up to 40 cm snow depth (Macfarlane et al., 2023); included are also additional measurements from previous Arctic campaigns during the 2004–2017 period documented in Confer et al. (2023).

[b]Estimates based on chemical composition measured with an Aerosol Chemical Speciation Monitor (ACSM) (see text; Gong et al., 2023).

($N_{0.5–20\ \mu m}$) are observed (**Figure 3c**), and their size and volume distributions are characterized during blowing snow and no-blowing snow periods (**Figure 4a** and **4b**).

A log-log plot depicting the aerosol particle size distribution during blowing snow and no-blowing snow periods is shown in **Figure 4a**. The number density for aerosol particles across the entire size range measured (d_p = 0.5–20 µm) is significantly higher when there is blowing snow, with less variability (indicated by the shaded region representing the 99% confidence interval). We observe more than an order of magnitude increase in the number density for aerosol particles larger than 10 µm and increases by a factor of 2–3 for particles smaller than 1 µm when there is blowing snow. The aerosol volume distribution (**Figure 4b**) shows two modes, one between 1 µm and 2 µm and the other between 6 µm and 10 µm, indicating that most of the aerosol mass resides in the super-micron range as expected for SSA.

A bar chart (**Figure 4c**) of the monthly mean aerosol number concentrations from December 2019 to April 2020 shows the seasonality and the impact blowing snow has on aerosol number concentration, with the error bars

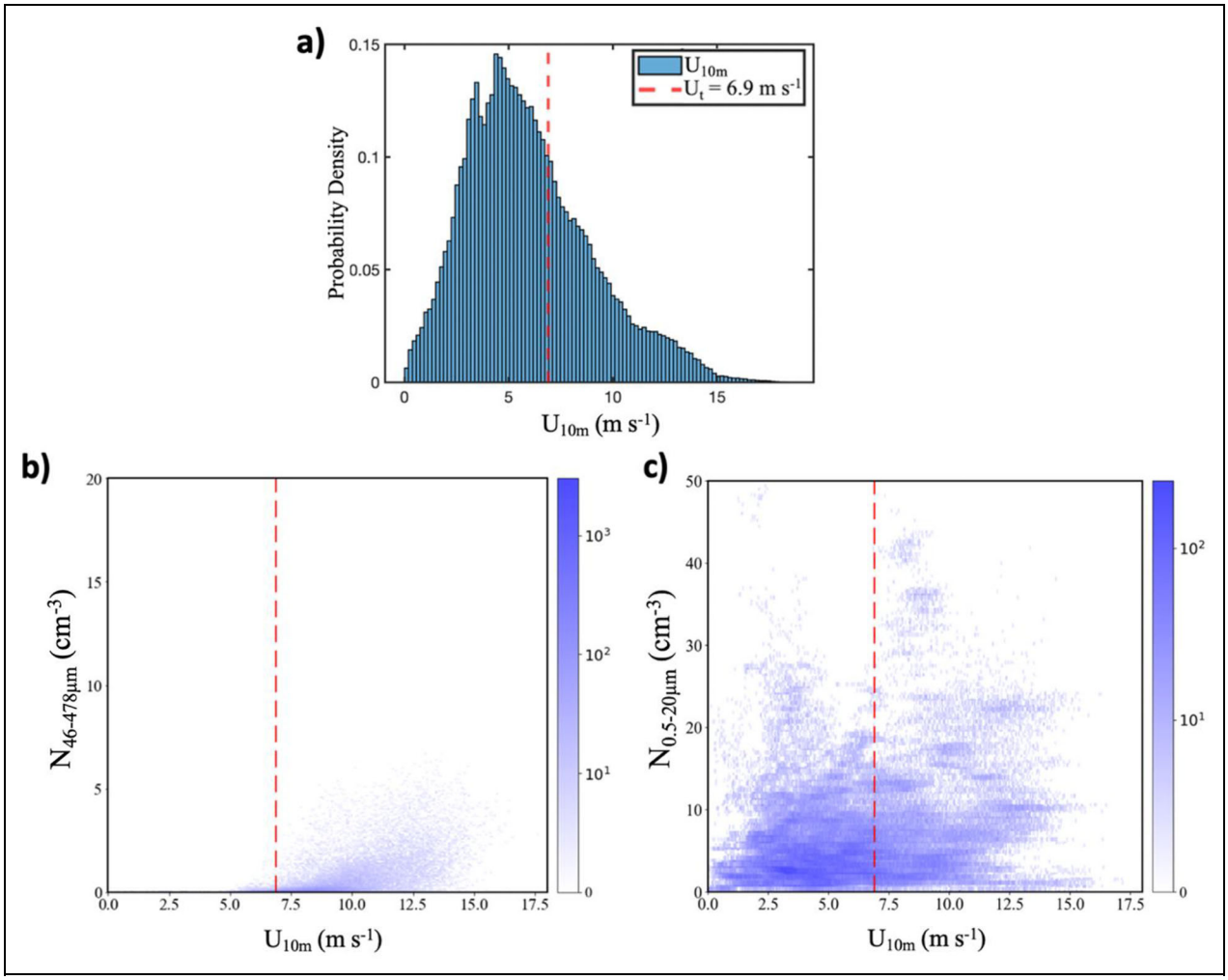

Figure 3. Wind speed, snow particle, and coarse aerosol concentrations during MOSAiC (October 2019 to May 2020). (a) Probability density of the 10-m wind speed ($U_{10\ m}$) with the empirical minimum threshold wind speed for blowing snow (=6.9 m s^{-1}) shown as a vertical dotted red line, (b) scatter plot of the total snow particle number concentration $N_{46–478\ \mu m}$ at ~0.08 m above the snow surface as a function of $U_{10\ m}$, and (c) scatter plot of the total coarse aerosol number concentration $N_{0.5–20\,\mu m}$ at 2 m above the snow surface as a function of $U_{10\ m}$. The color bars indicate the density of the data points.

showing the 99% confidence interval of the mean. Sub-micron particles (d_p = 0.5–1 μm) during blowing snow in December (~ 10 cm^{-3}) are more than double the number concentration than when there is no blowing snow (~4 cm^{-3}). Similarly, super-micron aerosol number concentration (d_p = 1–20 μm) in December is nearly 7 times higher when there is blowing snow. During the months of January, February, and March, the sub-micron aerosol number concentration increased by factors of 1.1, 1.7, and 2.3, respectively, while the super-micron aerosol number concentration increased by factors of 2, 1.8, and 2.5, respectively, during blowing snow periods. There is also a factor of 5 decrease in the super-micron aerosol number concentration from winter (December) to spring (March) during blowing snow periods. In April, however, we observe more super-micron aerosol during no-blowing snow periods. We speculate this could be long range transport of aerosol by advection or increased biological activity owed to the transition from winter to spring. Thus, these observations emphasize the seasonality of blowing snow and the impact it can have on the seasonal cycle of atmospheric aerosol concentration of large and small particles.

As a case study, we pick two periods, one during the Arctic winter phase (December 3–14, 2019; **Figure 5**) and another during the spring phase (March 21–31, 2020; **Figure 6**), to better understand the relationship between $U_{10\ m}$, snow particle, and aerosol number concentrations. For instance, from December 8, 2019, to December 12, 2019, the snow particle size spectrum shows a signal (**Figure 5b**), which directly corresponds to the time when the 10-m wind speed is above the threshold wind speed (**Figure 5a**) and RH_{ice} <100% (**Figure 5d**). During the same period, there is a corresponding increase in the coarse aerosol size range (d_p ranging from ~0.4 μm to 8 μm) with number concentrations as high as 60 cm^{-3} (**Figure 5c**). Estimates based on ACSM observations indicate that the sub-micron aerosol particles (d_p = 10–625 nm) detected during that time are comprised of

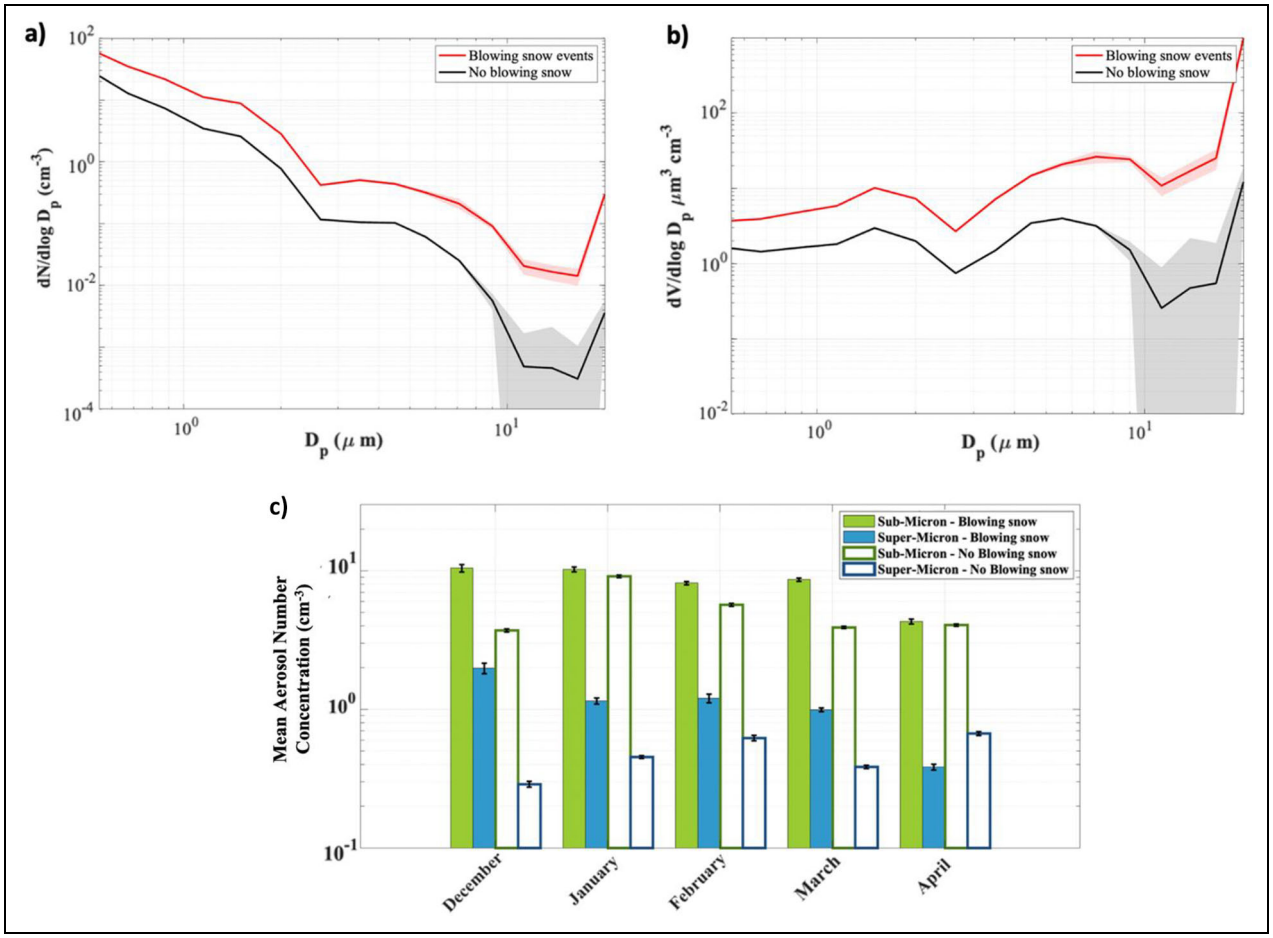

Figure 4. Coarse aerosol concentrations at 2 m during and outside periods of blowing snow. (a) Aerosol size distribution during blowing snow (when $U_{10\ m} > U_{t,10\ m}$ and detection of snow particles close to the surface) and no-blowing snow periods, with the shaded region representing the 99% confidence interval. (b) Aerosol volume distribution during blowing snow and no-blowing snow periods, with the shaded region representing the 99% confidence interval, and (c) monthly mean aerosol number concentration of sub-micron (d_p 0.5–1.0 μm) and super-micron (d_p 1.0–20 μm) aerosol particles from December 2019 to April 2020 during blowing snow (filled bars) and no-blowing snow periods (open bars). The error bars represent the 99% confidence interval.

up to 94% sea salt (**Figure 5a**). We also find a strong correlation between $U_{10\ m}$ and the proportion of sea salt in sub-micron aerosol particles ($R = 0.61$, $P < 0.05$). This is one example of how increased wind speed results in snow being lofted from the surface and contributing under sub-saturated conditions to the formation of SSA. The super-micron aerosol particle chemical composition is not measured by the ACSM, but it is likely dominated by sea salt as well since the super-micron aerosol number concentration peaks at the same time as the sub-micron aerosol sodium chloride (NaCl) fraction (**Figure 5c**). ACSM data are not available outside the December 3–12, 2019, period, but we assume that sea salt contributes significantly to coarse aerosol also during December 2019 to May 2020. Similarly, during the spring period between March 26, 2020, and March 30, 2020, when $U_{10\ m} > U_t$ (**Figure 6a**), snow particle sizes as large as ~500 μm are detected at concentrations $>10^3$ cm^{-3} (**Figure 6b**). At the same time, as RH_{ice} dropped to values below 100% (**Figure 6d**), coarse aerosol particles (d_p = 0.5–20 μm) increased to number concentrations as high as 20 cm^{-3} (**Figure 6c**).

We also observe a temporal lag in the measurements, with snow particles being detected first, followed by the aerosol particle signal from the CLASP instrument (**Figure 5b** and **5c** and **Figure 6b** and **6c**). The time lag between the snow and aerosol number concentration could be because of saturated conditions and scavenging of the newly produced aerosol particles by larger snow particles. During the initial period of the blowing snow event in the early hours of December 8, 2019 (**Figure 5d**), the relative humidity with respect to ice (RH_{ice}) is less than 100%. This suggests that scavenging by snow could be causing the temporal lag between snow and aerosol particles. **Figure 6d** shows $RH_{ice} > 100\%$ from midday on March 26, suggesting a lack of significant aerosol particle production via sublimation during this period, and possibly particle scavenging followed by deposition.

These are 2 examples of how blowing snow results in the formation of coarse aerosol under subsaturated conditions. Detailed time series plots for the entire December 2019–May 2020 period are included in the Supplemental Material (Figures S1–S16). In the following sections, we

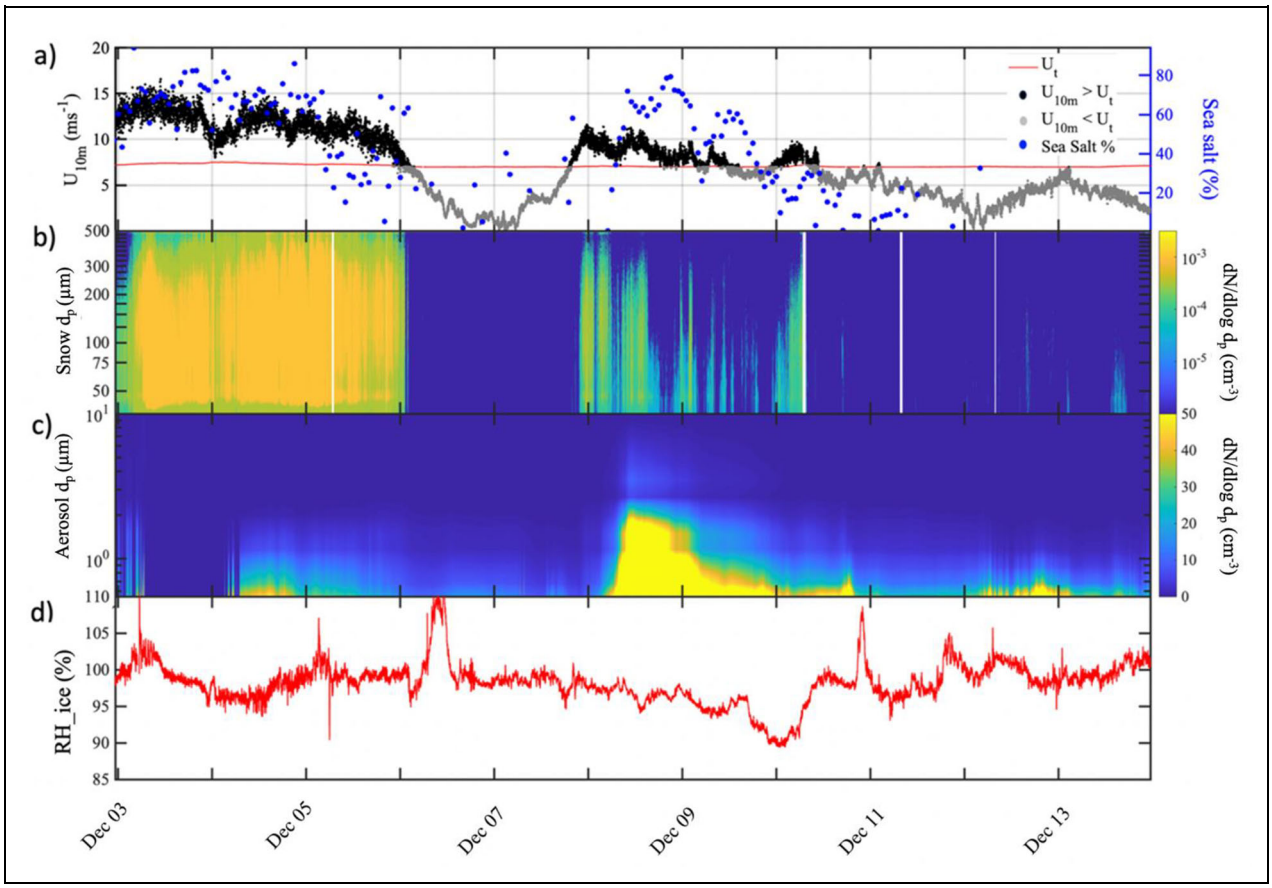

Figure 5. Time series representations from the Arctic winter phase during MOSAiC (December 3–12, 2019). (a) The 10-m wind speed ($U_{10\ m}$) alongside the threshold wind speed ($U_{t,10\ m}$) (Equation 4; Li and Pomeroy, 1997), mass fraction of sea salt in sub-micron aerosol particles (d_p = 10–625 nm); (b) the size distribution of snow particles (dN/dlogd_p) within a diameter range of 46–478 µm at ~0.08 m above the snow; (c) the size distribution of coarse aerosol (dN/dlogd_p) within a diameter range of 0.5–20 µm at 2 m above the snow; and (d) relative humidity with respect to ice (RH_{ice}).

first identify the sensitivity of key climate variables to SSA production from blowing snow and then use the entire dataset to parameterize the process.

3.2. Sensitivity analysis

Both first order and total Sobol indices show that the shape parameter α dominates the sensitivity of the parameterization and controls SSA number flux (**Figure 7**). The first order Sobol Index for α (0.55) is significantly higher than for any other parameter. Considering the total Sobol indices to account for the interaction between parameters, we find that α still dominates the sensitivity of the parameterization with a total Sobol Index value of 0.96. Note that the previously observed range for α between 2 and 11 (Frey et al., 2020) is broad, reflecting a large range of skewness in the blowing snow particle size distribution. α has been shown to vary horizontally and vertically throughout the atmosphere (Nishimura and Nemoto, 2005) but remains poorly constrained due to sparse measurements. Due to the large sensitivity of the blowing snow parameterization to α, better constraints from observations appear to be critical for model validation (Yang et al., 2019), as well as climate model implementation and projections.

SSA number flux is also sensitive to RH_{ice}, snow particle diameter (d_p), $U_{10\ m}$, and snow age with total Sobol indices between 0.1 and 0.2 (**Figure 7**). Roughness length RL has been found to have small contribution to the model sensitivity because it is only used to calculate the friction velocity (u^*), which in turn is used to calculate the saltation layer blowing snow mixing ratio (q_{bsalt}) in Equation 3. Notably, SSA number flux is not sensitive to snow salinity (S_p) in the range considered, though dry NaCl particle's size formed will be affected. This is in contrast to SSA mass flux (in Equation 1), which has been shown to linearly depend on snow salinity (Yang et al., 2008; 2019). This motivates a parameterization of S_p as a function of a more widely available parameter such as snow depth as done by Confer et al. (2023) and in this study (see Section 3.5).

3.3. Threshold wind speed during MOSAiC

Observed and empirical threshold wind speeds calculated with Equation 4 for the onset of drifting and blowing snow during MOSAiC as well as N-ICE2015 and the Weddell Sea are shown as a function of ambient temperature at 2 m (**Figure 8**). Following the approach of Frey et al. (2020), the onset of drifting or blowing snow is defined as the moment when snow drift density µ near the snow

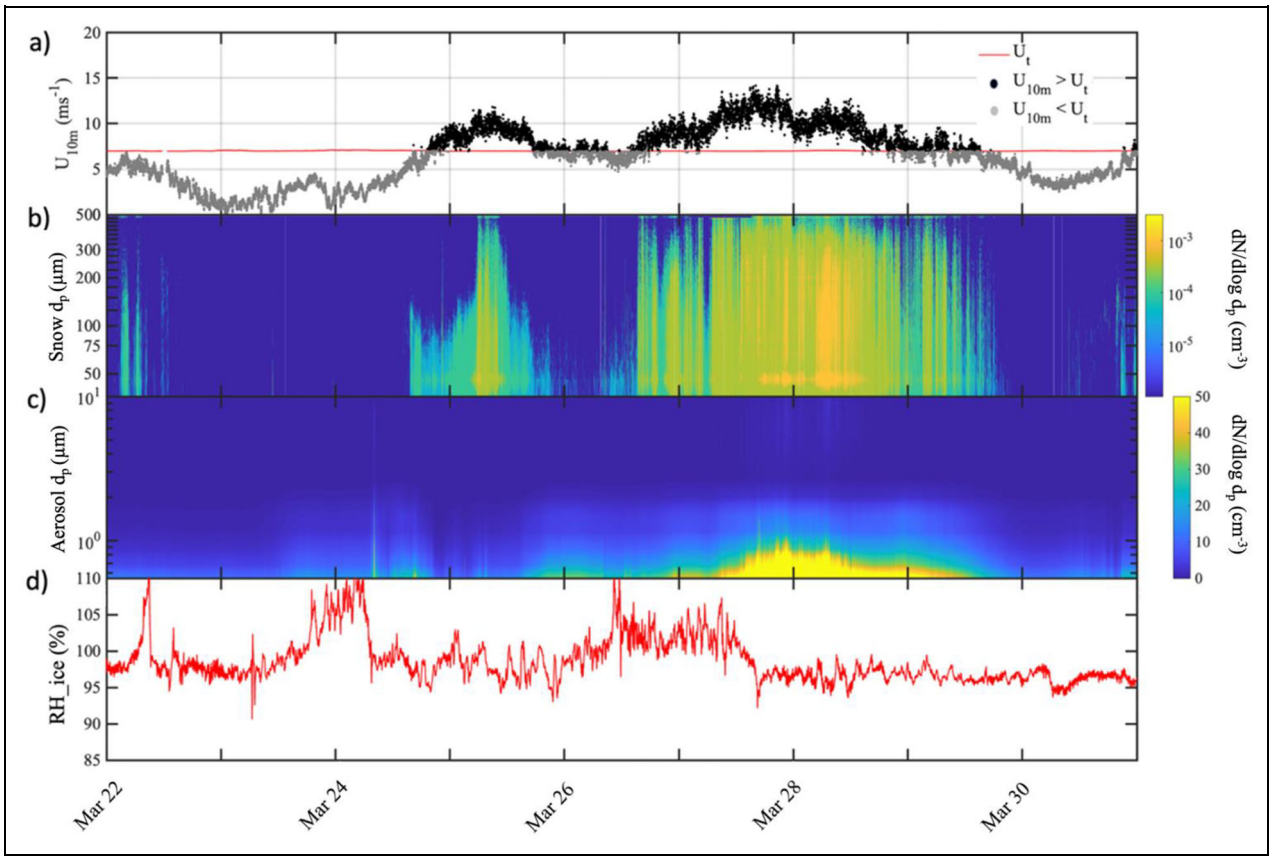

Figure 6. Time series representations from the Arctic spring phase during MOSAiC (March 21–31, 2020). (a) The 10-m wind speed ($U_{10\ m}$) alongside the threshold wind speed ($U_{t,10\ m}$) (Equation 4; Li and Pomeroy, 1997); (b) the size distribution of snow particles (dN/dlogd_p) within a diameter range of 46–478 μm at ∼0.08 m above the snow; (c) the size distribution of coarse aerosol (dN/dlogd_p) within a diameter range of 0.5–20 μm at 2 m above the snow; and (d) relative humidity with respect to ice (RH_{ice}).

surface exceeds a critical value μ_c (=0.0001 kg m^{-3}). The snow drift density is calculated as $\mu = 4/3\ \pi\rho_{ice} \int N_s(d_p) (d_p/2)^3\ d d_p$ with the density of ice ρ_{ice} (=917 kg m^{-3}) and the measured snow particle spectral number density N_s. Choosing this particular value of μ_c reduced contributions from noise. In addition, comparison with snow drift densities observed at 10 m, when available, allowed to exclude precipitation-only events and select particle increases dominated by lofting from the surface.

During MOSAiC, the observed mean $\pm 1\sigma$ $U_{t,10\ m}$ for drifting and blowing snow was 7.6 ± 2.1 (range 1.9–14.2) m s^{-1} (**Table 4**). In general, most observed $U_{t,10\ m}$ values during MOSAiC and also during N-ICE2015 and in the Weddell Sea fall within the $\pm 1\sigma$ range of predictions by the empirical parameterization of Li and Pomeroy (1997) (Equation 4; **Figure 8**). However, instances when observed $U_{t,10\ m}$ values are outside the $\pm 1\sigma$ range indicate that the true drift threshold wind speed can be significantly higher (18% of all values during MOSAiC) or lower (13% of all values during MOSAiC) than predicted (**Figure 8**). This is merely a reflection of the limitations of Equation 4, since other than temperature, salinity and snow grain morphology may also influence bonding strength and wind energy required for snow particle uplift. But we still consider Equation 4 a robust model to predict the onset of blowing snow. It is worth to note that observed $U_{t,10\ m}$ values at the lower end of the range overlap with onset wind speeds of sea spray production generally considered to be 4 m s^{-1} (Monahan and O'Muircheartaigh, 1986). This makes source attribution of aerosol to either blowing snow or open leads at wind speeds between 4 m s^{-1} and the empirical minimum $U_{t,10\ m}$ of 6.9 m s^{-1} at −27°C ambiguous (Chen et al., 2022). Other parameters are required to disentangle relative contributions from these 2 wind-driven aerosol sources.

3.4. Snow particle size distribution

The snow particle size distribution varies with altitude and wind speed (Nishimura et al., 2014; Frey et al., 2020). For instance, with an increase in wind speed, the mean diameter of the blown snow particles increases, but with an increase in altitude, the mean diameter of the snow particles decreases because of the gravitational settling of larger particles. Therefore, the parameters α and β (Equation 5) should be a function of wind speed and altitude. Using a constant value of the shape and scale parameter does not accurately represent the size distribution of snow particles under varying wind speeds. Using the MOSAiC observations, we derive below a wind speed-dependent expression for the values of α and β near the snow surface.

Using snow particle size distributions and 10-m wind speed data at 1-min resolution, we fit a gamma distribution to the data to derive parameters α and β for every

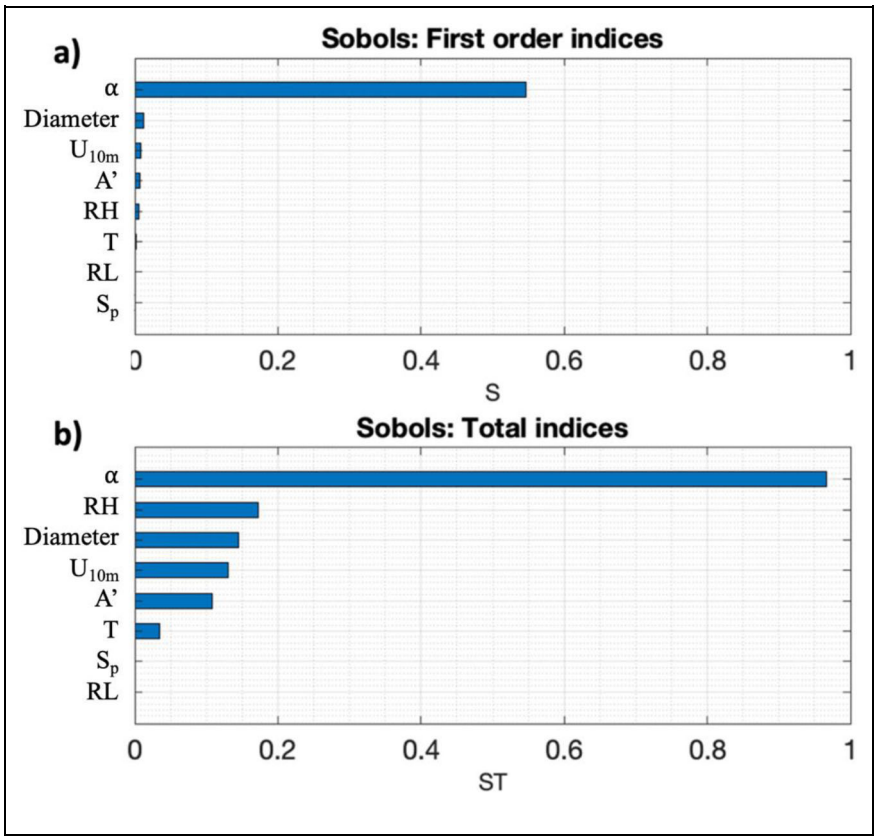

Figure 7. Sensitivities of blowing snow model parameters. Computed (a) first order Sobol's indices (S_i) and (b) total Sobol indices ($S_{T,i}$) of parameters driving the SSA number flux from blowing snow using the respective parameter ranges from **Table 2**.

wind speed bin of width 0.1 m s^{-1} (**Figure 9a**). We notice that the gamma distribution fit lies within the interquartile range of the observations; however, the fit does underpredict the mean diameter consistently across the entire observational dataset. This is because fitting a gamma distribution to observations produces a continuous size spectrum, including particles below the SPC size detection limit of 36 μm, thereby lowering the mean particle diameter. Although the fit is within the interquartile range, it does not capture the decreasing trend when $U_{10\ m}$ is between 5.7 m s^{-1} and 7.5 m s^{-1}, that is, below the mean observed threshold wind speed $U_{t,10\ m}$ of 7.6 m s^{-1} (**Table 4**). We hypothesize the reason for this large mean diameter between 5.7 m s^{-1} and 7.5 m s^{-1} could be precipitation of large snow crystals or that this wind speed range might correspond to a transitional wind speed range where the dynamics of snow particle aggregation change. At these wind speeds, there could be optimal conditions for snow particles to collide and stick together, leading to the formation of larger aggregates (Comola et al., 2017). This aggregation mechanism could result in an increase in mean particle diameter. As wind speeds increase beyond this range, the higher turbulence and shear might break apart these aggregated snow particles, leading to smaller particle sizes. Additionally, the gamma distribution, while adept at capturing size distributions of suspended snow particles, may not account for these localized aggregation effects. Therefore, the observed higher mean diameter in this specific wind speed range could be a result of enhanced snow particle aggregation and depends on the snow composition and dynamics which we don't have information on, so we can only hypothesize.

We use an exponential and logarithmic function (shown in Equations 8 and 9) to parameterize α and β, respectively, as a function of $U_{10\ m}$. The exponential fit for α (R^2 = 0.95; **Figure 9b**) and the logarithmic fit for β (R^2 = 0.94; **Figure 9c**) are both statistically robust. We notice that α is better constrained than past studies, with its values ranging between 1.9 and 3.1 (**Figure 9b**). Moreover, the shape parameter α reaches a constant value of ~1.9 at wind speeds larger than 10 m s^{-1}, while the scale parameter β still increases with increasing wind speeds. This phenomenon indicates that (i) the production and the loss of small size blowing snow particles reach a steady state when winds are strong enough (>10 m s^{-1}) and (ii) a further increase in wind speeds only generates large particles, as both beta and mean diameter increase. The above results imply that the production and loss rates of blowing snow particles are determined by specific microphysical processes, which are not fully clear yet and require future research. The parameterizations for α and β are shown in Equations 8 and 9 (where $U_{10\ m}$ > 5.7 m s^{-1}):

$$\alpha = 11.58 * \exp(-0.428 * U_{10\ m}) + 1.911 \quad (8)$$

$$\beta = 37.97 * \log(0.38 * U_{10\ m}) \quad (9)$$

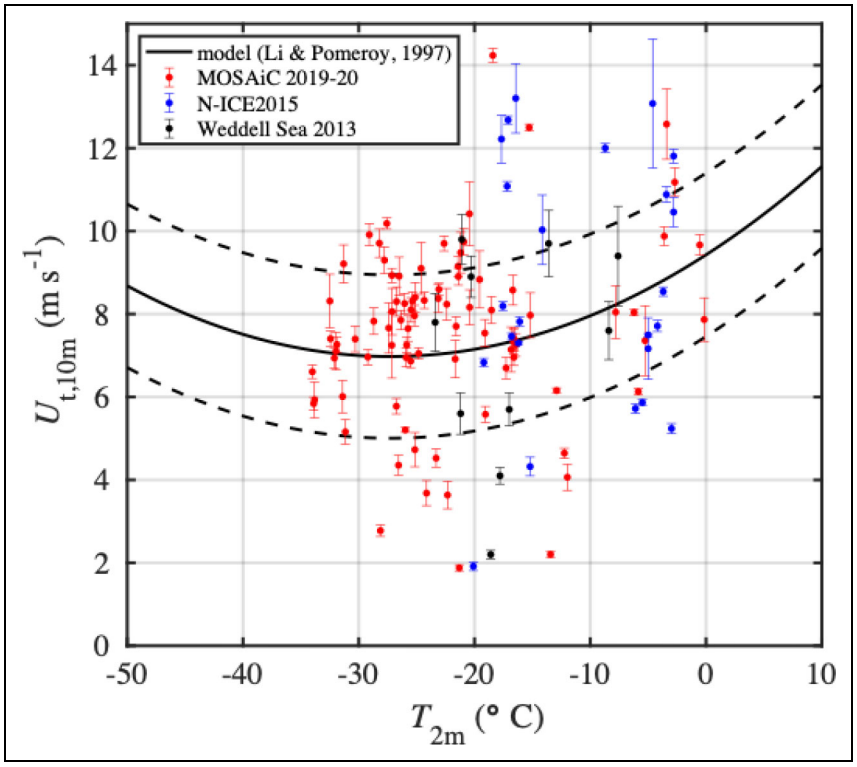

Figure 8. Threshold wind speed for drifting and blowing snow above sea ice at 10 m ($U_{t,10\ m}$) as a function of ambient temperature at 2 m ($T_{2\ m}$). Shown are 3- to 10-min means of observations in the Arctic (MOSAiC, N-ICE 2015) and Antarctic (Weddell Sea 2013, from Frey et al., 2020) centered on the time when the snow drift density μ near the snow surface exceeds a threshold of 0.0001 kg m^{-3} (symbols) with error bars indicating ±1 standard deviation. Observations are compared to $U_{t,10\ m}$ predicted by the temperature-dependent parameterization of Li and Pomeroy (1997) (solid line; Equation 4) with the dashed lines indicating the range of ±1 standard error.

Table 4. Snow drift threshold wind speeds above sea ice observed in the Arctic (MOSAiC, N-ICE2015) and Weddell Sea, Antarctica

Location	$T_{2\ m}$ (°C) Mean ±1σ (Range)	$U_{t,10\ m}$ (m s^{-1}) Mean ±1σ (Range)	*N* (Number of Events)[a]
MOSAiC (October 2019–May 2020)	−21.9 ± 8.2 (−34.0 to −0.2)	7.6 ± 2.1 (1.9 to 14.2)	85
N-ICE2015 (March 2015)	−10.8 ± 6.5 (−20.1 to −2.8)	8.7 ± 3.0 (1.9 to 13.2)	24
Weddell Sea (June–July 2013)[b]	−16.9 ± 5.4 (−23.4 to −7.6)	7.1 ± 2.6 (2.2 to 9.8)	10

[a]Number of drift or blowing snow onsets as defined in Section 3.3. Note several drift onsets can occur during a blowing snow event lasting >10 h (see definition in Section 3.1).

[b]From Frey et al. (2020).

We validate the derived parameterizations Equations 8 and 9 against other available observations carried out with the same instrument as in this study. Both particle size range and bins detected are therefore the same as in this study. **Figure 10** shows observed and modeled mean snow particle diameter as a function of wind speed for both the N-ICE2015 campaign in the Arctic during March 1–17, 2015, and the Weddell Sea campaign in the Antarctic during June 21–August 5, 2013 (from Frey et al., 2020). For the comparison between observations and the parameterization, we consider only data above the observed mean threshold wind speeds $U_{t,10\ m}$ (vertical blue dashed lines in **Figure 10**) when lofted particles are expected to dominate over precipitating particles and not be affected by aggregation processes discussed above. The parameterization developed using the 8-month-long Arctic dataset from MOSAiC matched well with the N-ICE2015 observations also collected in the Arctic (**Figure 10a**). However, the parameterization systematically underpredicts the Antarctic measurements from the Weddell Sea, which show on average around 1.5 times larger particle diameters than the estimates (**Figure 10b**). Larger snow particle size at similar wind speed in the Antarctic are likely due to environmental conditions different to the Arctic, for example, differences

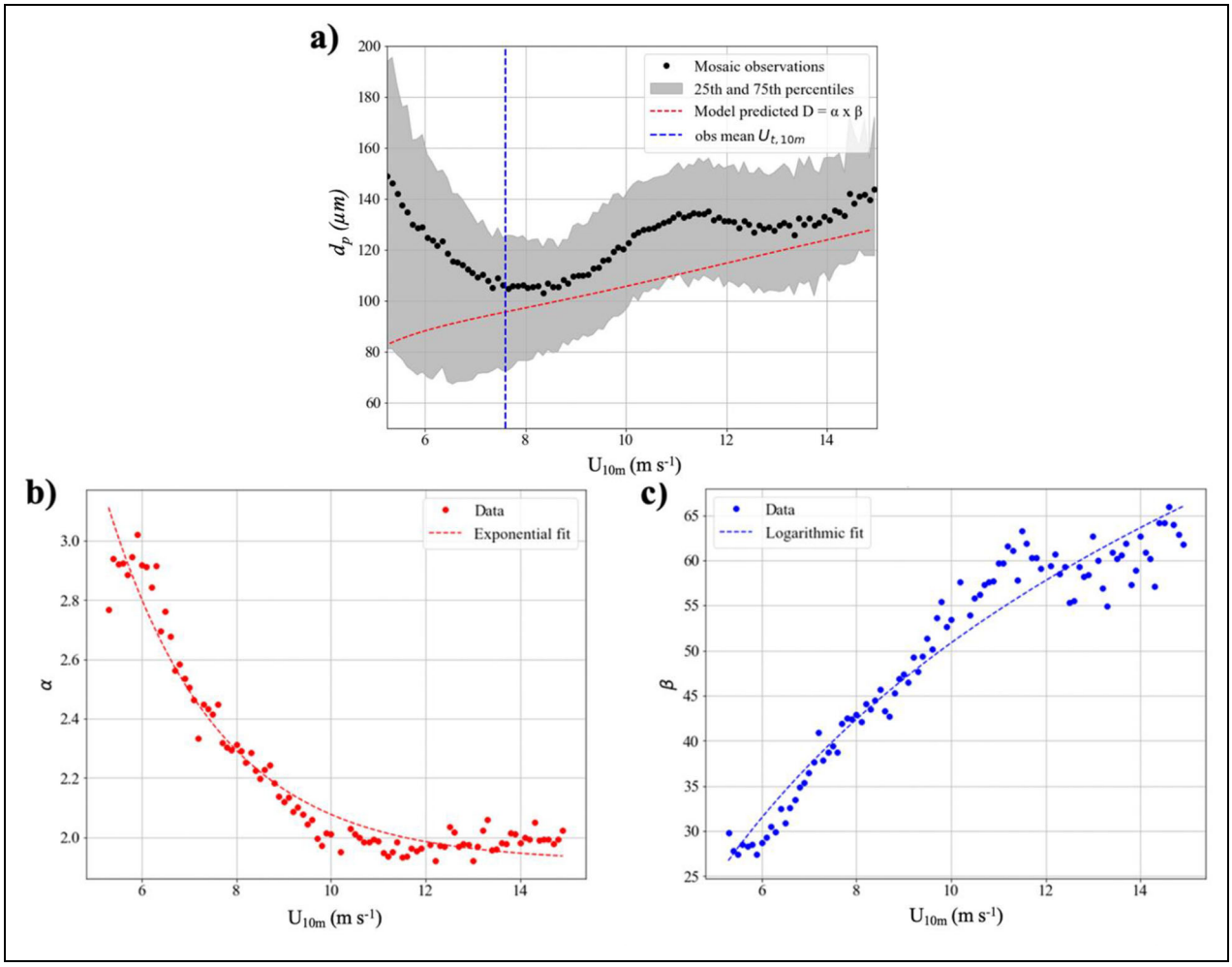

Figure 9. Observed and modeled mean snow particle diameters at ~0.08 m above the snowpack on sea ice. (a) Mean diameter of snow particles as a function of the 10-m wind speed ($U_{10\ m}$). The black symbols represent observations, with the shaded black regions illustrating the interquartile range. The dotted red line indicates estimates of d_p (=αβ) based on fitting a gamma distribution to observations and using Equations 8 and 9. (b) Estimates of shape parameter α with an exponential curve fit as a function of wind speed (from Equation 8) and (c) estimates of scale parameter β with a logarithmic curve fit as a function of wind speed (from Equation 9).

in meteorology (temperature, relative humidity) and sea ice underneath affecting snow grain metamorphism, and also precipitation. During blowing snow conditions in the Antarctic, precipitation did occur most of the time, likely contributing large particles and increasing the mean particle diameter near the surface (Frey et al., 2020), whereas during Arctic winter periods with very little or no precipitation occurred, making it likely that older snow particles at the top of the snowpack were mechanically reduced in size over the course of multiple drifting or blowing snow events.

In summary, the new parameterization of snow particle size distributions during blowing snow conditions is robust in the Arctic for wind speeds above the threshold for drift and blowing snow.

From the sensitivity analysis in Section 3.2, we showed that the blowing snow SSA number flux is most sensitive to α. The parameterizations we developed in Equations 8 and 9 result in a better constraint on α, which now ranges between 1.9 and 3.1 (**Figure 9**). We repeated the sensitivity analysis by constraining α between 1.9 and 3.1 to investigate the impact of the new parameterization on the sensitivity rankings of the other parameters using their first order (**Figure 11a**) and total Sobol indices (**Figure 11b**). We note that the SSA number flux from blowing snow is now most sensitive to 4 factors: relative humidity above ice RH_{ice}, $U_{10\ m}$, snow age, and temperature. Therefore, these factors are important to consider when implementing and analyzing new model estimates of SSA number flux using this parameterization.

3.5. Salinity probability distribution

Snow salinity S_p remains an important factor to consider as it impacts SSA mass flux and influences the SSA size distribution since the dry particle diameter of SSA generated by sublimation is a function of S_p to the power of 1/3 (Yang et al., 2008; 2019). Low snow salinity favors fine and ultra-fine SSA production; on the other hand, high snow salinity, for example, from frost flowers, will mostly form large SSA. Since the salinity probability distribution $\psi(S_p)$ varies regionally and seasonally (Massom et al., 2001), the

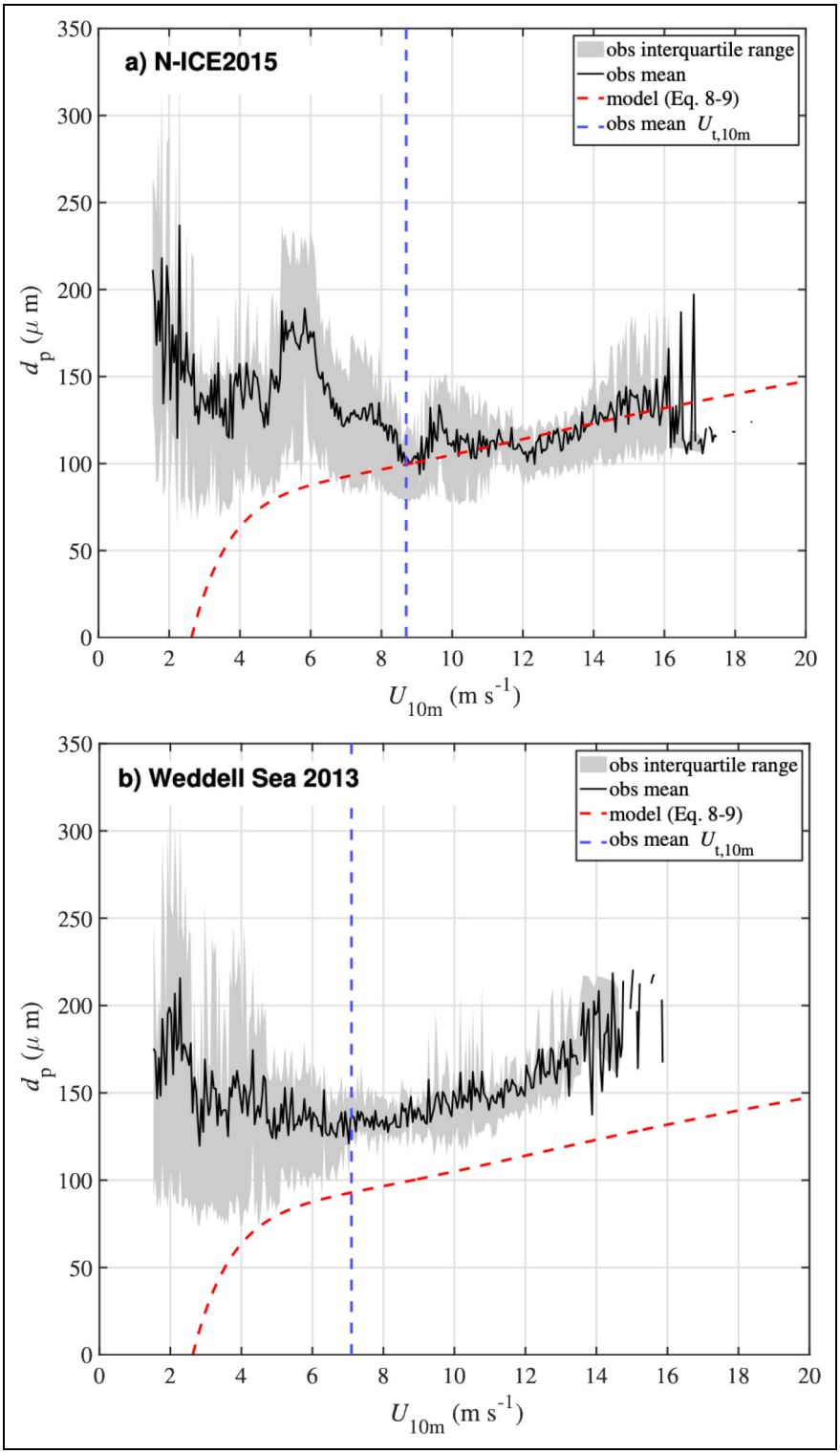

Figure 10. Mean diameter of snow particles at ~0.2 m above the snowpack on sea ice as a function of 10-m wind speed ($U_{10\ m}$) at other measurement locations. The bold black lines and shaded areas represent the mean diameter and interquartile range, respectively, from observations (a) in the Arctic during March 1–17, 2015 (N-ICE2015) and (b) in the Weddell Sea, Antarctica during June 21–August 5, 2013 (from Frey et al., 2020). The bold dotted blue lines represent the mean observed threshold wind speeds for drifting and blowing snow during the respective campaigns: 8.7 m s^{-1} for N-ICE2015 and 7.1 m s^{-1} for the Weddell Sea measurements (**Table 4**). The dotted red lines represent the estimate of mean snow particle diameter d_p (=αβ) using the parameterizations shown in Equations 8 and 9.

modeling of SSA from blowing snow requires characterizing a representative snow salinity probability distribution. **Figure 12** shows snow salinity as a function of snow depth (where 0 cm represents the snow–sea ice interface) with values from past studies in blue (Krnavek et al., 2012; Ewert et al., 2013; Nandan et al., 2017; Peterson et al.,

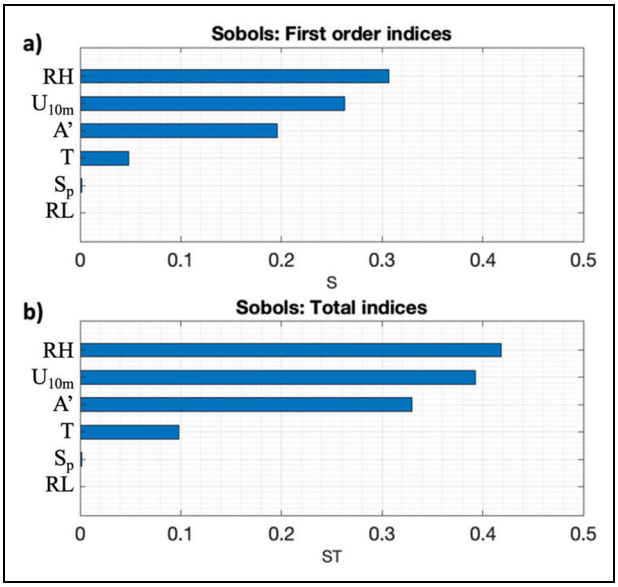

Figure 11. Sensitivities of blowing snow model parameters. (a) The first order and (b) total Sobol indices of parameters driving the SSA number flux from blowing snow using the respective parameter ranges from **Table 2**, except now constraining α and β with the new parameterization (Equations 8 and 9).

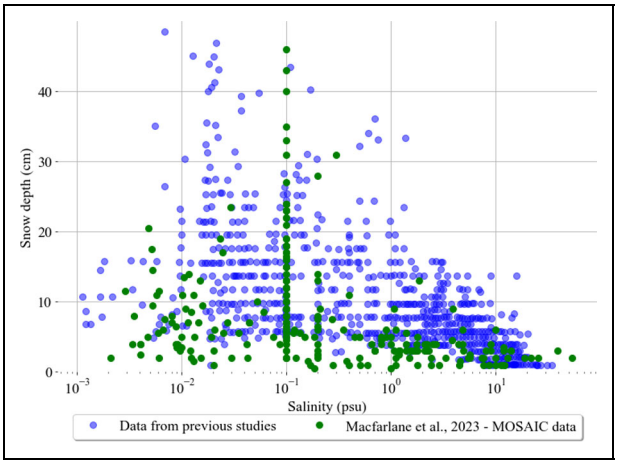

Figure 12. Relationship between snow salinity S_p and snow depth, where the datum (=0 cm) represents the snow–sea ice interface. Included are observations from MOSAiC expedition as green symbols (Macfarlane et al., 2023) and from past Arctic studies as blue symbols (Krnavek et al., 2012; Ewert et al., 2013; Nandan et al., 2017; Peterson et al., 2019; Confer et al., 2023).

2019; Confer et al., 2023) and in green from the MOSAiC campaign (Macfarlane et al., 2023). High salinities occur in snow that is very close (0–5 cm) to the snow–sea ice interface and keep decreasing further away from this interface due to the decreasing efficiency in the upward migration of brine into the snowpack (**Figure 12**).

The snow that is lofted from the surface during a blowing snow event will have a certain salinity distribution, which depends on the thickness of the snow layer lofted from the

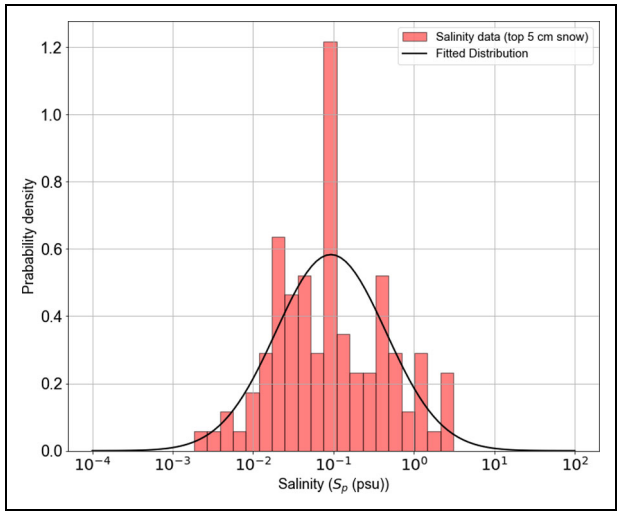

Figure 13. The probability density function for snow salinity S_p measurements and fitted normal distribution for the top 5 cm of snow (measured from the snow–air interface). Fitting a normal distribution results in a mean ± 1σ of 0.09 ± 4.8 psu, with a 95% confidence interval of 0.00–9.7 psu (**Table 5**).

Table 5. Parameters of a normal distribution fit to snow salinities S_p observed during MOSAiC (Macfarlane et al., 2023) as a function of snow layer thickness potentially lofted from the surface during storms (measured from the air–snow interface)

Snow Layer Thickness (cm)	Mean S_p (psu)	Standard Deviation σ of S_p (psu)	95% Confidence Interval of S_p (psu)	*N* sample size
5	0.09	4.8	0–9.7	107
10	0.14	7.1	0–14.2	234
15	0.25	8.9	0–17.8	547
20	0.48	11.2	0–22.4	834

surface and the total depth of the snowpack. As an example, assuming a total snowpack depth of 20 cm and lofting of the top 5 cm of snow, we characterize its salinity distribution in **Figure 13**. We use the Kolmogorov–Smirnov test to evaluate whether the distribution can be described by a normal distribution, where $P < 0.05$ would denote a good fit. In **Figure 13**, the distribution has a P value of less than 0.05, a mean S_p of 0.09 psu, and standard deviation of 4.8 psu, which corresponds to a S_p 95% confidence interval ranging from 0.004 to 2.1 psu (**Table 4**).

To illustrate how the snow salinity S_p distribution would change with the amount of snow lofted from the surface, we fit normal distributions to observed S_p. **Table 4** lists the parameters of the normal distribution fits ($P <$ 0.05) for the top 5 cm, 10 cm, 15 cm, and 20 cm of snow, and respective distributions are illustrated in **Figure 14**. We note that the distribution has the smallest mean

salinity for the top 5 cm of snow, and the thicker the layer of snow lofted the higher the mean salinity, which increases by 15% (for 10 cm), 41% (for 15 cm), and 69% (for 20 cm). For the simulations presented in the following sections, we utilize the salinity distribution derived from the entire MOSAiC dataset (mean $\pm$ 1σ = 0.19 $\pm$ 8.4 psu) (Macfarlane et al., 2023). The distribution is illustrated in the histogram shown in **Figure 14**.

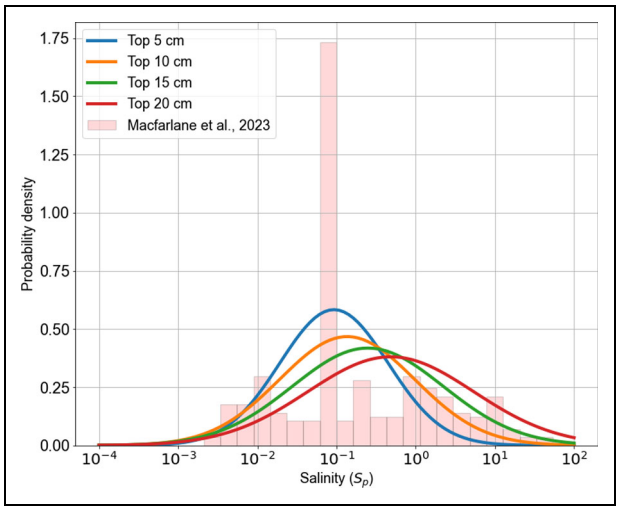

Figure 14. The snow salinity S_p distribution for the entire snowpack observed during MOSAiC (Macfarlane et al., 2023) and normal S_p distribution fits for different layer thicknesses of snow potentially lofted from the surface during storms (top 5–20 cm) (Table 5).

3.6. Applying the new SSA flux parameterization in p-TOMCAT

We implement the new parameterization from Equations 8 and 9 into the chemistry transport model p-TOMCAT and compare it to measurements made during the MOSAiC expedition. **Figure 15** shows the comparison between the MOSAiC observations and model simulations for aerosol number concentrations in the size range of 0.4–12 µm. The simulation with just the open ocean scheme (green line) does not capture the trend. However, the model simulations that include blowing snow aerosol source over sea ice capture the peaks much better. Overall, the simulation with the new scheme (SI-New Scheme) produces approximately 14% more particles than the old scheme (SI-Old Scheme) along the MOSAiC drift track. The OO scheme model output in comparison to observations exhibits a negative correlation coefficient of −0.07, suggesting a weak inverse relationship to observations over sea ice. In contrast, comparing the SI-New Scheme and SI-Old Scheme model outputs to observations reveals a positive correlation, with correlation coefficients R of 0.28 and 0.23, respectively, with the SI-New Scheme correlating slightly better. Comparing the simulated new scheme and measured sub- (0.4–1 µm) and super-micron (1–12 µm) aerosol number concentration, we estimate correlation coefficients to be 0.26 and 0.25, respectively. The new blowing snow scheme developed in this study was also applied in a past study (Gong et al., 2023) using GEOS-Chem (for particles in the size range of 0.01–1 µm), which also showed improvements in correlation coefficient from 0.43 (simulation with only SSA from open ocean) to 0.53 (simulation with the new blowing snow scheme). Overall, including the blowing snow scheme improves agreement with observations, albeit with low

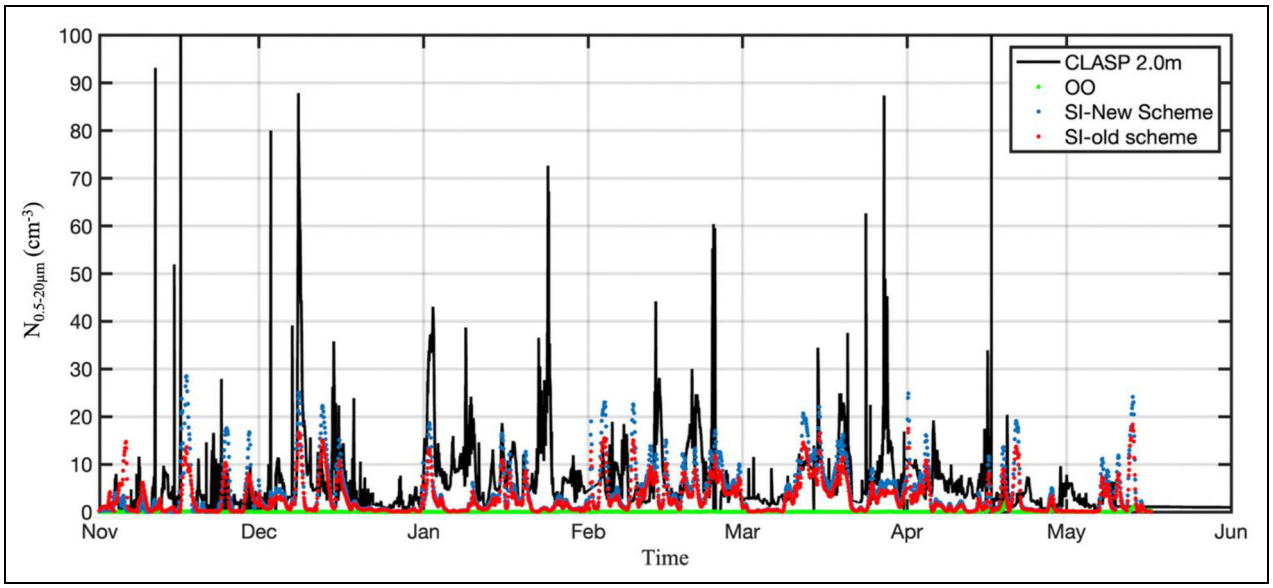

Figure 15. Observed and modeled aerosol number concentrations during MOSAiC. Comparison between observed total aerosol number concentration $N_{0.5–20\,\mu m}$ (black line) and model predictions of coarse aerosol for similar size bins (green line: only open ocean sourced SSA; blue line: open ocean and sea ice sourced SSA using the old parameterization after Yang et al. [2019]; red line: open ocean and sea ice sourced SSA using the new parameterization from this study).

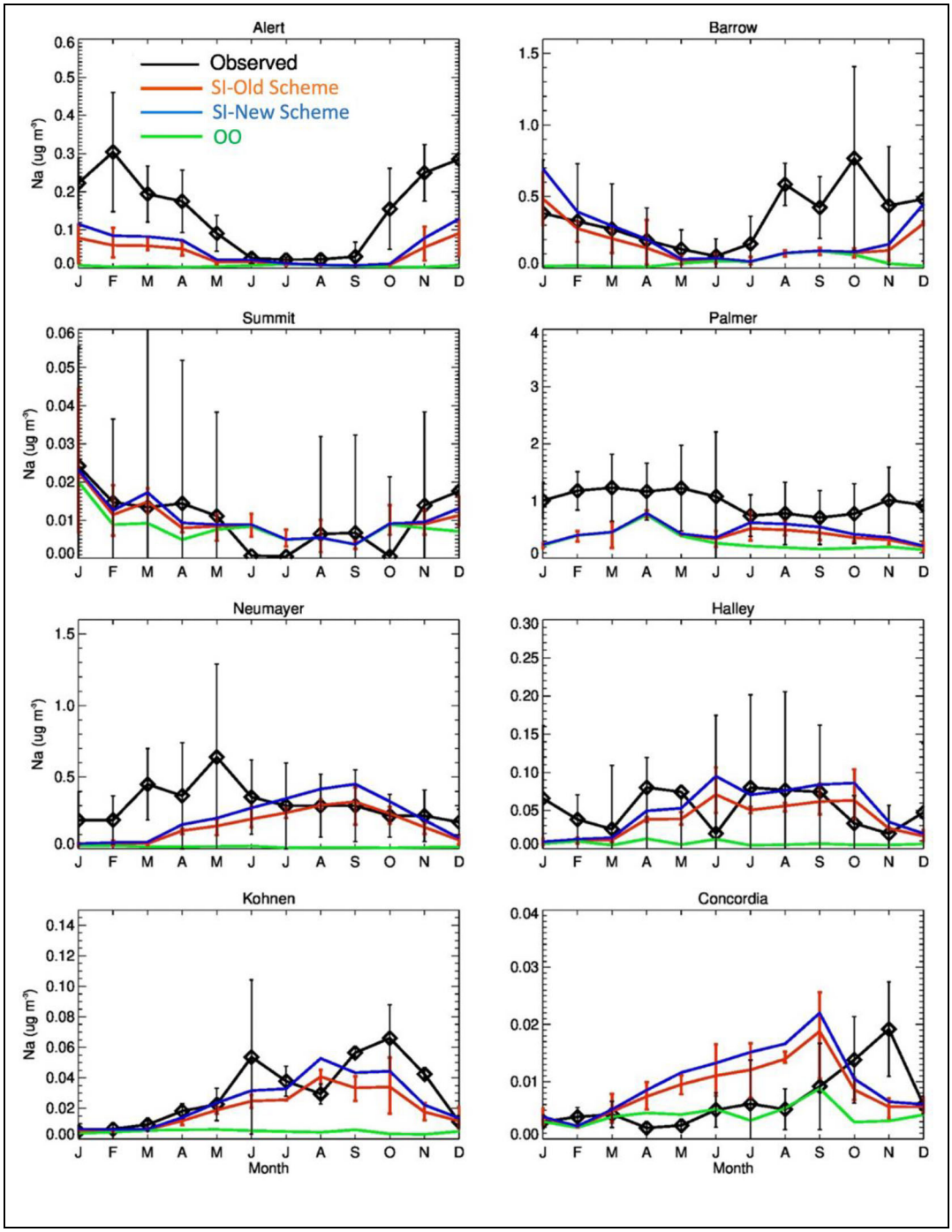

Figure 16. Comparison of the sodium mass concentration between the observations at several polar research stations and model simulations. Green line: SSA only from open ocean, red line: SSA from open ocean and blowing snow using the old parameterization after Yang et al. (2019), and blue line: SSA from open ocean and blowing snow using the new parameterization from this study. The mass concentration of modeled SSA is for particle diameters 0.02–10 μm.

correlation coefficients. Low *R* values are not surprising because the p-TOMCAT model only computes SSA, whereas coarse aerosol observed in the 0.5–20 μm size range also contains contributions from non-SSA particles, in particular during Arctic haze periods in winter. Though the model's performance has improved by including blowing snow schemes, there is still room for research to refine the model to improve its reliability in predicting observed data in polar regions over sea ice.

We also compare the seasonal cycle between the model simulations and observations of sodium mass concentration at various polar research stations in the Arctic (Alert, Barrow, Summit) and Antarctic (Palmer, Neumayer, Halley, Kohnen, Concordia) as shown in **Figure 16**. We note that the OO parameterization cannot replicate the seasonal cycle of the sodium mass concentration. The simulations with blowing snow are much better at reproducing the seasonal cycle, like at Alert in the Arctic, albeit

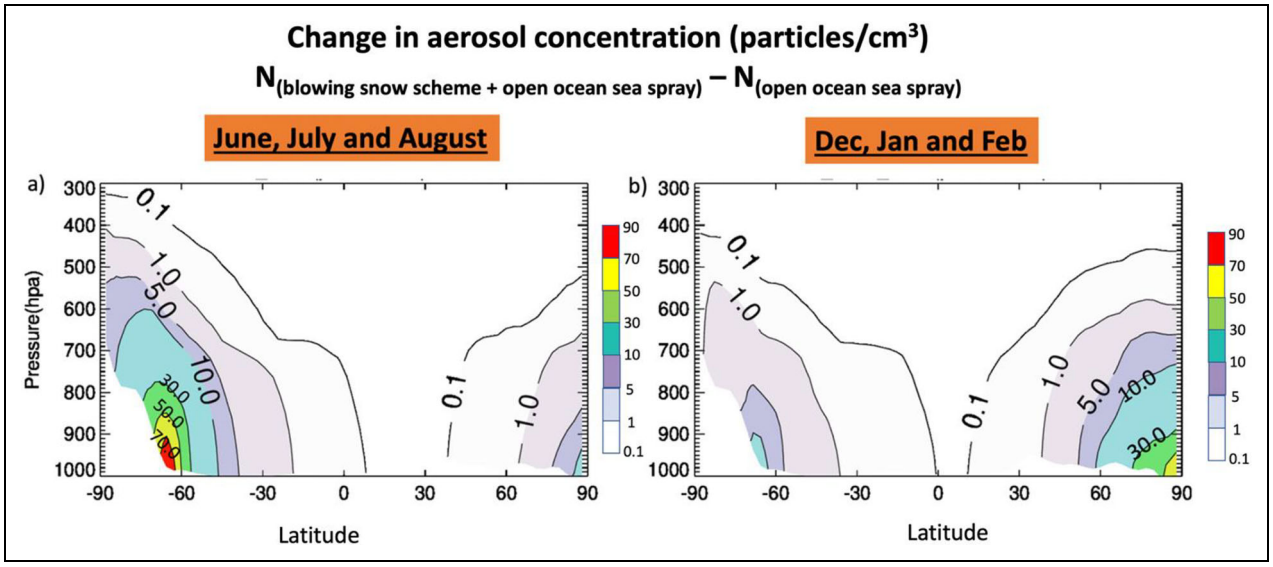

Figure 17. Contour visualization of the difference in total aerosol number concentration (cm^{-3}) (N) between a simulation with the new blowing snow parameterization ($N_{(\text{blowing snow scheme + open ocean sea spray})}$) and one without blowing snow ($N_{(\text{open ocean sea spray})}$). (a) Seasonal mean during June, July, and August and (b) seasonal mean during December, January, and February. The aerosol number concentration of modeled SSA is for particle diameters of 0.02–10 μm.

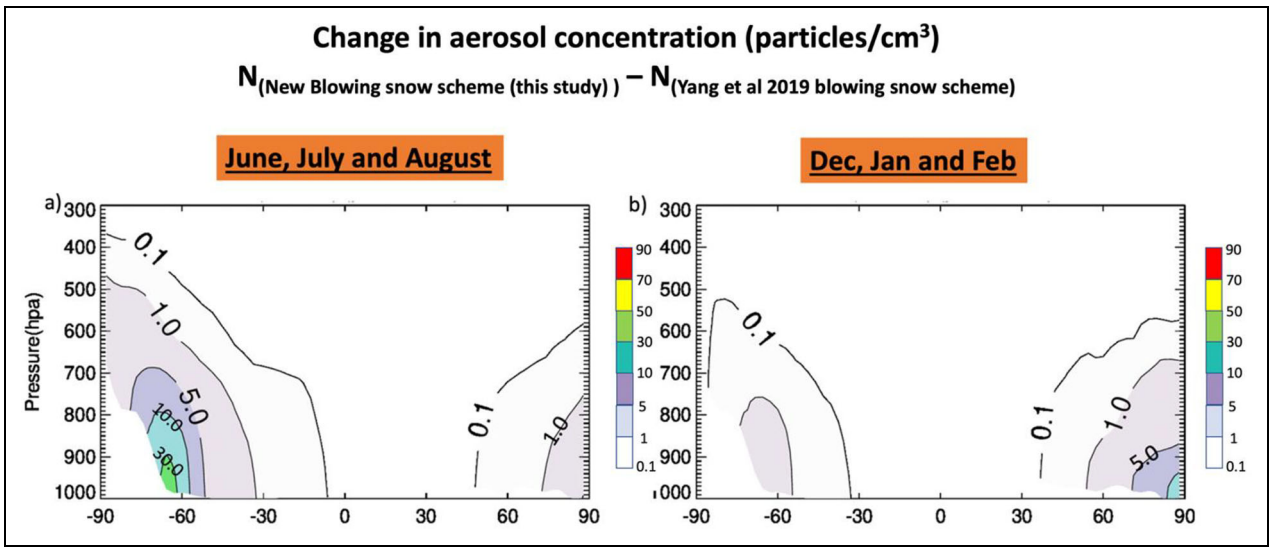

Figure 18. Change in aerosol number concentration between the new parameterization with wind speed-dependent α and β when compared to parameterization in a past study with fixed values of α and β (Yang et al., 2019). (a) Seasonal mean during June, July, and August, and (b) seasonal mean during December, January, and February.

underpredicting the Na mass concentration by a factor of 3 in February. At Antarctic research stations like Kohnen, the blowing snow simulations are within the standard deviation of the measurements, unlike the OO parameterization. The new blowing snow scheme from this study does produce a higher sodium concentration, which is expected since the scheme was shown to produce more SSA particles in comparison to Yang et al. (2019) (**Figure 18**).

Figure 17a shows a seasonal mean of the aerosol number concentration from blowing snow using the new parameterization during the Antarctic winter (June, July, and August ["JJA"]) and **Figure 17b** for the Arctic winter (December, January, and February ["DJF"]). The contour plot (**Figure 17a**) shows that there is around a maximum increase of ~70 cm^{-3} aerosol number concentration close to the surface up to 900 hpa in the Antarctic during winter. During Arctic winter, the aerosol number concentrations close to the surface increase by as much as ~50 cm^{-3}. The summertime increase in aerosol number concentration in the polar regions is moderate, going as high as 10 cm^{-3} in the Antarctic summer (**Figure 17b**). These values are consistent with some of the observed boundary layer aerosol measurements in the Antarctic at high wind speeds (>15 m s^{-1}),

where number concentrations range between 10 cm^{-3} and 100 cm^{-3} (Hara et al., 2014).

The new parameterization for α and β has also been compared to parameterizations from past studies where α (=2) and β (=70) are fixed (Yang et al., 2019). The difference between the seasonal mean in the aerosol number concentration between these two parameterizations is shown in **Figure 18**. The new parameterization produces more particles, with wintertime aerosol number concentration in the Antarctic increasing by up to 30 cm^{-3} and in the Arctic increasing by up to 10 cm^{-3}, in comparison to the Yang et al. (2019) scheme. Given the pristine nature of polar regions, a small change in aerosol number concentration can have a substantial impact on the radiation balance, and this study motivates the need to include this mechanism in general circulation models to better characterize polar aerosol and improve climate projections and aerosol radiative forcing estimates.

Thus, the new scheme has been shown to produce more aerosol particles than the old blowing snow scheme and is able to reproduce the sodium seasonal cycle much more accurately that the open ocean simulations. The difference in aerosol concentration estimated by the new scheme can have a significant effect on climate in the pristine polar regions, whose radiation balance is very sensitive to changes in aerosol concentration.

4. Conclusions

We analyzed in situ measurements above the sea ice of snow particle size distributions, coarse aerosol number concentrations, snow salinity, and meteorology during the MOSAiC expedition 2019–2020. During the December 2019–May 2020 period, a total of 26 blowing snow events occurred, covering about 20–40% of time per month subject to blowing snow conditions. Blowing snow led to increases in coarse aerosol number concentrations by up to an order of magnitude compared to no-blowing snow periods. Available observations of particle NaCl mass fraction indicate that sea salt contributed significantly to total observed coarse aerosol. A sensitivity analysis showed that the total SSA number flux from blowing snow is most sensitive to shape factor α of the snow particle size distribution. We used the MOSAiC measurements to characterize the SSA that originates via the sublimation of blowing snow and to further constrain the snow particle size distribution parameters. The snow particle distribution varies as a function of wind speed following a 2-parameter gamma distribution. We developed exponential and logarithmic parameterizations for shape and scale factor α and β as a function of the 10-m wind speed, which both show a high correlation with the measurements with R^2 values of 0.95 and 0.94, respectively. Values of β increased with increasing wind speed, whereas α was found to range between 1.9 and 3 approaching a constant value of $\sim$1.9 at wind speeds >10 m s^{-1}. Comparison to other polar observations showed that the new parameterization of snow particle size distributions during blowing snow conditions is robust in the Arctic for wind speeds above the threshold for drift and blowing snow. We implement the updated parameterization into the chemistry transport model p-TOMCAT. Including a blowing snow aerosol source resulted in a significant increase in wintertime aerosol number concentrations in polar regions compared to the open ocean-only simulations, with increases as high as 70 cm^{-3} in the Antarctic and 50 cm^{-3} in the Arctic. When compared to the old scheme, the new parameterization produced 14% more aerosol particles along the MOSAiC cruise track, captured trends in coarse aerosol number concentrations during MOSAiC slightly better, and was also able to reproduce the seasonal cycle in sodium concentration across several polar research stations. Thus, this scheme helps model the SSA production from blowing snow more accurately than past studies and adds new knowledge to improve our understanding of aerosol particles in polar regions. This study will inform future modeling work in polar regions, which needs to account for blowing snow as a significant source of aerosol particles, especially in winter and early spring. The pristine nature of polar regions renders its atmosphere highly sensitive to perturbations in aerosol concentration. Incorporating this new SSA scheme into a climate model would be the next step in our research, and implementation of this parameterization using the UK Earth System Model will be part of a future study. This will improve quantifying the sweeping impacts of blowing snow on both polar and global climate.

Data accessibility statement

All model output and measurements of snow particle and aerosol number densities and wind speed used in this study can be accessed at https://doi.org/10.5281/zenodo.13760111. Met City meteorological data are available from the post-processed files ("Level 3" files) as documented in Cox et al. (2023). Snow salinity data were retrieved from Confer et al. (2023) and Macfarlane et al. (2023). Data for the chemical composition of the submicron aerosol measured by the ACSM in the ARM container during MOSAiC were retrieved from Gong et al. (2023). Weddell Sea data were published previously (Frey et al., 2020; https://doi.org/10.5285/853dd176-bc7a-48d4-a6be-33bcc0f17eeb).

Supplemental material

The supplemental files for this article can be found as follows:

Supplemental Material (docx)

Acknowledgments

Data used in this manuscript originates from field work carried out as part of the international Multidisciplinary drifting Observatory for the Study of Arctic Climate (MOSAiC) with the tag MOSAiC20192020. We thank all persons involved in the expedition of the RV *Polarstern* during MOSAiC in 2019–2020 (AWI PS122 00) as listed in Nixdorf et al. (2021). We are grateful for instrument support to ensure continuous year-round sampling during MOSAiC, in particular to Amélie Kirchgäßner, Matthew Shupe, Taneil Uttaal, Laurianne Quélévere, Ivo Beck, and Tuija Jokinen. We are thankful also to Ian Brooks for providing the CLASP instrument and support. Some data were obtained from the Atmospheric Radiation Measurement (ARM) User Facility, a U.S. Department of

Energy (DOE) Office of Science User Facility Managed by the Biological and Environmental Research Program. We would like to thank the British Antarctic Survey for providing computational support. We also thank members of the H2020 CRiceS project for providing advice and engaging in scientific discussion during the drafting of this manuscript.

Funding

AR, XY, TL-C, and MMF were supported by the European Union's Horizon 2020 research and innovation program under grant agreement no. 101003826 via project CRiceS (Climate Relevant interactions and feedbacks: the key role of sea ice and Snow in the polar and global climate system), the UK Natural Environment Research Council (NERC) (NE/S00257X/1, NE/M005852/1, NE/J021172/1), and the NERC National Capability International grant SURface FluxEs In AnTarctica (SURFEIT) (NE/X009319/1). XG was supported by the Research Center for Industries of the Future (RCIF) at Westlake University. DGP was supported by the UK Natural Environment Research Council (NERC) (NE/T006331/1) grant Southern Ocean Clouds.

Competing interests

All authors declare that they have no conflict of interest.

Author contributions

AR, XY, and MMF are responsible for the drafting and scientific analysis performed in the manuscript. MMF designed and carried out the field experiments in the Antarctic and Arctic with support from the respective expedition teams and processed the data. ED and DGP performed parameter sensitivity analysis shown in Sections 3.2 and 3.4. XG provided guidance on the usage of the chemical composition data collected using the ACSM instrument. XY performed the model simulations. TL-C provided feedback during the drafting of the manuscript. AR and MMF wrote the manuscript with contributions from all co-authors.

References

Abram, NJ, **Wolff, EW**, **Curran, MAJ.** 2013. A review of sea ice proxy information from polar ice cores. *Quaternary Science Reviews* **79**: 168–183. DOI: http://dx.doi.org/10.1016/j.quascirev.2013.01.011.

Albrecht, BA. 1989. Aerosols, cloud microphysics, and fractional cloudiness. *Science* **245**(4923): 1227–1230. DOI: http://dx.doi.org/10.1126/science.245.4923.1227.

Andreas, EL, **Persson, POG**, **Grachev, AA**, **Jordan, RE**, **Horst, TW**, **Guest, PS**, **Fairall, CW.** 2010. Parameterizing turbulent exchange over sea ice in winter. *Journal of Hydrometeorology* **11**(1): 87–104. DOI: http://dx.doi.org/10.1175/2009JHM1102.1.

Beck, I, **Angot, H**, **Baccarini, A**, **Dada, L**, **Quéléver, L**, **Jokinen, T**, **Laurila, T**, **Lampimäki, M**, **Bukowiecki, N**, **Boyer, M**, **Gong, X**, **Gysel-Beer, M**, **Petäjä, T**, **Wang, J**, **Schmale, J.** 2022. Automated identification of local contamination in remote atmospheric composition time series. *Atmospheric Measurement Techniques* **15**(14): 4195–4224. DOI: http://dx.doi.org/10.5194/amt-15-4195-2022.

Bellouin, N, **Quaas, J**, **Gryspeerdt, E**, **Kinne, S**, **Stier, P**, **Watson-Parris, D**, **Boucher, O**, **Carslaw, KS**, **Christensen, M**, **Daniau, AL**, **Dufresne, JL**, **Feingold, G**, **Fiedler, S**, **Forster, P**, **Gettelman, A**, **Haywood, JM**, **Lohmann, U**, **Malavelle, F**, **Mauritsen, T**, **McCoy, DT**, **Myhre, G**, **Mülmenstädt, J**, **Neubauer, D**, **Possner, A**, **Rugenstein, M**, **Sato, Y**, **Schulz, M**, **Schwartz, SE**, **Sourdeval, O**, **Storelvmo, T**, **Toll, V**, **Winker, D**, **Stevens, B.** 2020. Bounding global aerosol radiative forcing of climate change. *Reviews of Geophysics* **58**(1): e2019RG000660. DOI: http://dx.doi.org/10.1029/2019RG000660.

Box, JE, **Bromwich, DH**, **Bai, LS.** 2004. Greenland ice sheet surface mass balance 1991–2000: Application of Polar MM5 mesoscale model and in situ data. *Journal of Geophysical Research: Atmospheres* **109**(D16): 1–21. DOI: http://dx.doi.org/10.1029/2003JD004451.

Budd, WF, **Dingle, WRJ**, **Radok, U.** 1966. The Byrd snow drift project: Outline and basic results. *Studies in Antarctic Meteorology* **9**: 71–134. DOI: http://dx.doi.org/10.1029/ar009p0071.

Carslaw, KS, **Lee, LA**, **Reddington, CL**, **Pringle, KJ**, **Rap, A**, **Forster, PM**, **Mann, GW**, **Spracklen, DV**, **Woodhouse, MT**, **Regayre, LA**, **Pierce, JR.** 2013. Large contribution of natural aerosols to uncertainty in indirect forcing. *Nature* **503**: 67–71. DOI: http://dx.doi.org/10.1038/nature12674.

Cascajo-Castresana, M, **Morin, S**, **Bittner, AM.** 2021. The ice-vapour interface during growth and sublimation. *Atmospheric Chemistry and Physics* **21**(24): 18629–18640. DOI: http://dx.doi.org/10.5194/acp-21-18629-2021.

Chen, Q, **Mirrielees, JA**, **Thanekar, S**, **Loeb, NA**, **Kirpes, RM**, **Upchurch, LM**, **Barget, AJ**, **Lata, NN**, **Raso, ARW**, **McNamara, SM**, **China, S**, **Quinn, PK**, **Ault, AP**, **Kennedy, A**, **Shepson, PB**, **Fuentes, JD**, **Pratt, KA.** 2022. Atmospheric particle abundance and sea salt aerosol observations in the springtime Arctic: A focus on blowing snow and leads. *Atmospheric Chemistry and Physics* **22**(23): 15263–15285. DOI: http://dx.doi.org/10.5194/acp-22-15263-2022.

Clarke, AD, **Owens, SR**, **Zhou, J.** 2006. An ultrafine sea-salt flux from breaking waves: Implications for cloud condensation nuclei in the remote marine atmosphere. *Journal of Geophysical Research: Atmospheres* **111**(D6): 148–227. DOI: http://dx.doi.org/10.1029/2005JD006565.

Comola, F, **Kok, JF**, **Gaume, J**, **Paterna, E**, **Lehning, M.** 2017. Fragmentation of wind-blown snow crystals. *Geophysical Research Letters* **44**(9): 4195–4203. DOI: http://dx.doi.org/10.1002/2017GL073039.

Confer, KL, **Jaeglé, L**, **Liston, GE**, **Sharma, S**, **Nandan, V**, **Yackel, J**, **Ewert, M**, **Horowitz, HM.** 2023. Impact of changing Arctic sea ice extent, sea ice age, and snow depth on sea salt aerosol from blowing snow and the open ocean for 1980–2017. *Journal of Geophysical Research: Atmospheres* **128**(3): e2022JD037667. DOI: http://dx.doi.org/10.1029/2022JD037667.

Cox, CJ, **Gallagher, MR**, **Shupe, MD**, **Persson, POG**, **Solomon, A**, **Fairall, CW**, **Ayers, T**, **Blomquist, B**, **Brooks, IM**, **Costa, D**, **Grachev, A**, **Gottas, D**, **Hutchings, JK**, **Kutchenreiter, M**, **Leach, J**, **Morris, SM**, **Morris, V**, **Osborn, J**, **Pezoa, S**, **Preußer, A**, **Riihimaki, LD**, **Uttal, T.** 2023. Continuous observations of the surface energy budget and meteorology over the Arctic sea ice during MOSAiC. *Scientific Data* **10**(1): 519. DOI: http://dx.doi.org/10.1038/s41597-023-02415-5.

de Leeuw, G, **Andreas, EL**, **Anguelova, MD**, **Fairall, CW**, **Lewis, ER**, **O'Dowd, C**, **Schulz, M**, **Schwartz, SE.** 2011. Production flux of sea spray aerosol. *Reviews of Geophysics* **49**(2): RG2001. DOI: http://dx.doi.org/10.1029/2010RG000349.

DeMott, PJ, **Hill, TCJ**, **McCluskey, CS**, **Prather, KA**, **Collins, DB**, **Sullivan, RC**, **Ruppel, MJ**, **Mason, RH**, **Irish, VE**, **Lee, T**, **Hwang, CY**, **Rhee, TS**, **Snider, JR**, **McMeeking, GR**, **Dhaniyala, S**, **Lewis, ER**, **Wentzell, JJ**, **Abbatt, J**, **Lee, C**, **Sultana, CM**, **Ault, AP**, **Axson, JL**, **Diaz Martinez, M**, **Venero, I**, **Santos-Figueroa, G**, **Stokes, MD**, **Deane, GB**, **Mayol-Bracero, OL**, **Grassian, VH**, **Bertram, TH**, **Bertram, AK**, **Moffett, BF**, **Franc, GD.** 2016. Sea spray aerosol as a unique source of ice nucleating particles. *Proceedings of the National Academy of Sciences of the United States of America* **113**(21): 5797–5803. DOI: http://dx.doi.org/10.1073/pnas.1514034112.

Déry, SJ, **Yau, MK.** 1999. A bulk blowing snow model. *Boundary-Layer Meteorology* **93**: 237–251. DOI: http://dx.doi.org/10.1023/A:1002065615856.

Déry, SJ, **Yau, MK.** 2001. Simulation of blowing snow in the Canadian Arctic using a double-moment model. *Boundary-Layer Meteorology* **99**: 297–316. DOI: http://dx.doi.org/10.1023/A:1018965008049.

Ewert, M, **Carpenter, SD**, **Colangelo-Lillis, J**, **Deming, JW.** 2013. Bacterial and extracellular polysaccharide content of brine-wetted snow over Arctic winter first-year sea ice. *Journal of Geophysical Research: Oceans* **118**(2): 726–735. DOI: http://dx.doi.org/10.1002/jgrc.20055.

Fan, SM, **Jacob, DJ.** 1992. Surface ozone depletion in Arctic spring sustained by bromine reactions on aerosols. *Nature* **359**: 522–524. DOI: http://dx.doi.org/10.1038/359522a0.

Frey, M, **Norris, S**, **Brooks, I**, **Anderson, P**, **Nishimura, K**, **Yang, X**, **Jones, A**, **Nerentorp Mastromonaco, M**, **Jones, D**, **Wolff, E.** 2019. Concentration, size distribution and chemical composition of snow particles, sea salt aerosol and snow on sea ice in the Weddell Sea (Antarctica) during austral winter/spring 2013. UK Polar Data Centre, Natural Environment Research Council, UK Research & Innovation. DOI: https://doi.org/10.5285/853dd176-bc7a-48d4-a6be-33bcc0f17eeb.

Frey, MM, **Norris, SJ**, **Brooks, IM**, **Anderson, PS**, **Nishimura, K**, **Yang, X**, **Jones, AE**, **Nerentorp Mastromonaco, MG**, **Jones, DH**, **Wolff, EW.** 2020. First direct observation of sea salt aerosol production from blowing snow above sea ice. *Atmospheric Chemistry and Physics* **20**(4): 2549–2578. DOI: http://dx.doi.org/10.5194/acp-20-2549-2020.

Gao, Z, **Geilfus, NX**, **Saiz-Lopez, A**, **Wang, F.** 2022. Reproducing Arctic springtime tropospheric ozone and mercury depletion events in an outdoor mesocosm sea ice facility. *Atmospheric Chemistry and Physics* **22**(3): 1811–1824. DOI: http://dx.doi.org/10.5194/acp-22-1811-2022.

Gong, SL. 2003. A parameterization of sea-salt aerosol source function for sub- and super-micron particles. *Global Biogeochemical Cycles* **17**(4): 1097. DOI: http://dx.doi.org/10.1029/2003gb002079.

Gong, X, **Zhang, J**, **Croft, B**, **Yang, X**, **Frey, MM**, **Bergner, N**, **Chang, RYW**, **Creamean, JM**, **Kuang, C**, **Martin, RV**, **Ranjithkumar, A**, **Sedlacek, AJ**, **Uin, J**, **Willmes, S**, **Zawadowicz, MA**, **Pierce, JR**, **Shupe, MD**, **Schmale, J**, **Wang, J.** 2023. Arctic warming by abundant fine sea salt aerosols from blowing snow. *Nature Geoscience* **16**(9): 768–774. DOI: http://dx.doi.org/10.1038/s41561-023-01254-8.

Graham, RM, **Itkin, P**, **Meyer, A**, **Sundfjord, A**, **Spreen, G**, **Smedsrud, LH**, **Liston, GE**, **Cheng, B**, **Cohen, L**, **Divine, D**, **Fer, I**, **Fransson, A**, **Gerland, S**, **Haapala, J**, **Hudson, SR**, **Johansson, AM**, **King, J**, **Merkouriadi, I**, **Peterson, AK**, **Provost, C**, **Randelhoff, A**, **Rinke, A**, **Rösel, A**, **Sennéchael, N**, **Walden, VP**, **Duarte, P**, **Assmy, P**, **Steen, H**, **Granskog, MA.** 2019. Winter storms accelerate the demise of sea ice in the Atlantic sector of the Arctic Ocean. *Scientific Reports* **9**(1): 9222. DOI: http://dx.doi.org/10.1038/s41598-019-45574-5.

Graham, RM, **Rinke, A**, **Cohen, L**, **Hudson, SR**, **Walden, VP**, **Granskog, MA**, **Dorn, W**, **Kayser, M**, **Maturilli, M.** 2017. A comparison of the two Arctic atmospheric winter states observed during N-ICE2015 and SHEBA. *Journal of Geophysical Research: Atmospheres* **122**(11): 5716–5737. DOI: http://dx.doi.org/10.1002/2016JD025475.

Granskog, MA, **Assmy, P**, **Gerland, S**, **Spreen, G**, **Steen, H**, **Smedsrud, LH.** 2016. Arctic research on thin ice: Consequences of Arctic sea ice loss. *Eos Transactions American Geophysical Union (United States)* **97**(5): 22–26. DOI: http://dx.doi.org/10.1029/2016eo044097.

Hara, K, **Hayashi, M**, **Yabuki, M**, **Shiobara, M**, **Nishita-Hara, C.** 2014. Simultaneous aerosol measurements of unusual aerosol enhancement in the troposphere over Syowa Station, Antarctica. *Atmospheric Chemistry and Physics* **14**(8): 4169–4183. DOI: http://dx.doi.org/10.5194/acp-14-4169-2014.

Hara, K, **Matoba, S**, **Hirabayashi, M**, **Yamasaki, T.** 2017. Frost flowers and sea-salt aerosols over seasonal sea-ice areas in northwestern Greenland during winter-spring. *Atmospheric Chemistry and Physics* **17**(13): 8577–8598. DOI: http://dx.doi.org/10.5194/acp-17-8577-2017.

Hara, K, **Osada, K**, **Yabuki, M**, **Yamanouchi, T.** 2012. Seasonal variation of fractionated sea-salt particles on the Antarctic coast. *Geophysical Research Letters* **39**(18): 18801. DOI: http://dx.doi.org/10.1029/2012GL052761.

Hill, KD, **Dauphinee, TM**, **Woods, DJ.** 1986. The extension of the Practical Salinity Scale 1978 to low salinities. *IEEE Journal of Oceanic Engineering* **11**(1): 109–112. DOI: http://dx.doi.org/10.1109/JOE.1986.1145154.

Hill, MK, **Brooks, BJ**, **Norris, SJ**, **Smith, MH**, **Brooks, IM**, **de Leeuw, G.** 2008. A Compact Lightweight Aerosol Spectrometer Probe (CLASP). *Journal of Atmospheric and Oceanic Technology* **25**(11): 1996–2006. DOI: http://dx.doi.org/10.1175/2008JTECHA1051.1.

Huang, J, **Jaeglé, L.** 2017. Wintertime enhancements of sea salt aerosol in polar regions consistent with a sea ice source from blowing snow. *Atmospheric Chemistry and Physics* **17**(5): 3699–3712. DOI: http://dx.doi.org/10.5194/acp-17-3699-2017.

Jaeglé, L, **Quinn, PK**, **Bates, TS**, **Alexander, B**, **Lin, JT.** 2011. Global distribution of sea salt aerosols: New constraints from in situ and remote sensing observations. *Atmospheric Chemistry and Physics* **11**(7): 3137–3157. DOI: http://dx.doi.org/10.5194/acp-11-3137-2011.

Jambon-Puillet, E, **Shahidzadeh, N**, **Bonn, D.** 2018. Singular sublimation of ice and snow crystals. *Nature Communications* **9**(1): 4191. DOI: http://dx.doi.org/10.1038/s41467-018-06689-x.

King, JC, **Anderson, PS.** 1994. Heat and water vapour fluxes and scalar roughness lengths over an Antarctic ice shelf. *Boundary-Layer Meteorology* **69**: 101–121. DOI: http://dx.doi.org/10.1007/BF00713297.

Krnavek, L, **Simpson, WR**, **Carlson, D**, **Domine, F**, **Douglas, TA**, **Sturm, M.** 2012. The chemical composition of surface snow in the Arctic: Examining marine, terrestrial, and atmospheric influences. *Atmospheric Environment* **50**: 349–359. DOI: http://dx.doi.org/10.1016/j.atmosenv.2011.11.033.

Krumpen, T, **Birrien, F**, **Kauker, F**, **Rackow, T**, **Von Albedyll, L**, **Angelopoulos, M**, **Jakob Belter, H**, **Bessonov, V**, **Damm, E**, **Dethloff, K**, **Haapala, J**, **Haas, C**, **Harris, C**, **Hendricks, S**, **Hoelemann, J**, **Hoppmann, M**, **Kaleschke, L**, **Karcher, M**, **Kolabutin, N**, **Lei, R**, **Lenz, J**, **Morgenstern, A**, **Nicolaus, M**, **Nixdorf, U**, **Petrovsky, T**, **Rabe, B**, **Rabenstein, L**, **Rex, M**, **Ricker, R**, **Rohde, J**, **Shimanchuk, E**, **Singha, S**, **Smolyanitsky, V**, **Sokolov, V**, **Stanton, T**, **Timofeeva, A**, **Tsamados, M**, **Watkins, D.** 2020. The MOSAiC ice floe: Sediment-laden survivor from the Siberian shelf. *The Cryosphere* **14**(7): 2173–2187. DOI: http://dx.doi.org/10.5194/tc-14-2173-2020.

Lapere, R, **Thomas, JL**, **Marelle, L**, **Ekman, AML**, **Frey, MM**, **Lund, MT**, **Makkonen, R**, **Ranjithkumar, A**, **Salter, ME**, **Samset, BH**, **Schulz, M**, **Sogacheva, L**, **Yang, X**, **Zieger, P.** 2023. The representation of sea salt aerosols and their role in polar climate within CMIP6. *Journal of Geophysical Research: Atmospheres* **128**(6): 1–36. DOI: http://dx.doi.org/10.1029/2022jd038235.

Legrand, M, **Yang, X**, **Preunkert, S**, **Theys, N.** 2016. Year-round records of sea salt, gaseous, and particulate inorganic bromine in the atmospheric boundary layer at coastal (Dumont d'Urville) and central (Concordia) East Antarctic sites. *Journal of Geophysical Research: Atmospheres* **121**(2): 997–1023. DOI: http://dx.doi.org/10.1002/2015JD024066.

Levine, JG, **Yang, X**, **Jones, AE**, **Wolff, EW.** 2014. Sea salt as an ice core proxy for past sea ice extent: A process-based model study. *Journal of Geophysical Research: Atmospheres* **119**(9): 5737–5756. DOI: http://dx.doi.org/10.1002/2013JD020925.

Li, L, **Pomeroy, JW.** 1997. Estimates of threshold wind speeds for snow transport using meteorological data. *Journal of Applied Meteorology and Climatology* **36**(3): 205–213. DOI: http://dx.doi.org/10.1175/1520-0450(1997)036<0205:EOTWSF>2.0.CO;2.

Macfarlane, AR, **Schneebeli, M**, **Dadic, R**, **Tavri, A**, **Immerz, A**, **Polashenski, C**, **Krampe, D**, **Clemens-Sewall, D**, **Wagner, DN**, **Perovich, DK**, **Henna-Reetta, H**, **Raphael, I**, **Matero, I**, **Regnery, J**, **Smith, MM**, **Nicolaus, M**, **Jaggi, M**, **Oggier, M**, **Webster, MA**, **Lehning, M**, **Kolabutin, N**, **Itkin, P**, **Naderpour, R**, **Pirazzini, R**, **Hämmerle, S**, **Arndt, S**, **Fons, S.** 2023. A database of snow on sea ice in the central Arctic collected during the MOSAiC expedition. *Scientific Data* **10**(1): 398. DOI: http://dx.doi.org/10.1038/s41597-023-02273-1.

Macfarlane, AR, **Schneebeli, M**, **Dadic, R**, **Wagner, DN**, **Arndt, S**, **Clemens-Sewall, D**, **Hammerle, S**, **Hannula, HR**, **Jaggi, M**, **Kolabutin, N**, **Krampe, D**, **Lehning, M**, **Matero, I**, **Nicolaus, M**, **Oggier, M**, **Pirazzini, R**, **Polashenski, C**, **Raphael, I**, **Regnery, J**, **Shimanchuck, E**, **Smith, MM**, **Tavri, A.** 2022. Snowpit salinity profiles during the MOSAiC expedition [dataset], in Macfarlane, AR, Schneebeli, M, Dadic, R, Wagner, DN, Arndt, S, Clemens-Sewall, D, Hammerle, S, Hannula, HR, Jaggi, M, Kolabutin, N, Krampe, D, Lehning, M, Matero, I, Nicolaus, M, Oggier, M, Pirazzini, R, Polashenski, C, Raphael, I, Regnery, J, Shimanchuck, E, Smith, MM, Tavri, A. 2021. Snowpit raw data collected during the MOSAiC expedition [dataset bundled publication]. PANGAEA. DOI: http://dx.doi.org/10.1594/PANGAEA.935934 and http://dx.doi.org/10.1594/PANGAEA.946807.

Marelle, L, **Thomas, JL**, **Ahmed, S**, **Tuite, K**, **Stutz, J**, **Dommergue, A**, **Simpson, WR**, **Frey, MM**, **Baladima, F.** 2021. Implementation and impacts of surface and blowing snow sources of Arctic bromine activation within WRF-chem 4.1.1. *Journal of Advances in Modeling Earth Systems* **13**(8): e2020MS002391. DOI: http://dx.doi.org/10.1029/2020MS002391.

Massom, RA, **Eicken, H**, **Haas, C**, **Jeffries, MO**, **Drinkwater, MR**, **Sturm, M**, **Worby, AP**, **Wu, X**, **Lytle, VI**, **Ushio, S**, **Morris, K**, **Reid, PA**, **Warren, SG**, **Allison, I.** 2001. Snow on Antarctic sea ice. *Reviews of Geophysics* **39**(3): 413–445. DOI: http://dx.doi.org/10.1029/2000RG000085.

McDougall, T, **Barker, PM.** 2011. Getting started with TEOS-10 and the Gibbs Seawater (GSW) Oceanographic Toolbox. SCOR/IAPSO Working Group 127.

Monahan, EC, **O'Muircheartaigh, IG**. 1986. Whitecaps and the passive remote sensing of the ocean surface. *International Journal of Remote Sensing* **7**(5): 627–642. DOI: http://doi.org/10.1080/01431168608954716.

Monahan, EC, **Spiel, DE**, **Davidson, KL.** 1983. A model of marine aerosol generation via whitecaps and wave disruption. *Oceanic Whitecaps* **2**: 167–174. DOI: http://dx.doi.org/10.1007/978-94-009-4668-2_16.

Nandan, V, **Geldsetzer, T**, **Yackel, J**, **Mahmud, M**, **Scharien, R**, **Howell, S**, **King, J**, **Ricker, R**, **Else, B.** 2017. Effect of snow salinity on CryoSat-2 Arctic first-year sea ice freeboard measurements. *Geophysical Research Letters* **44**(20): 10419–10426. DOI: http://dx.doi.org/10.1002/2017GL074506.

Ng, NL, **Herndon, SC**, **Trimborn, A**, **Canagaratna, MR**, **Croteau, PL**, **Onasch, TB**, **Sueper, D**, **Worsnop, DR**, **Zhang, Q**, **Sun, YL**, **Jayne, JT.** 2011. An Aerosol Chemical Speciation Monitor (ACSM) for routine monitoring of the composition and mass concentrations of ambient aerosol. *Aerosol Science and Technology* **45**(7): 780–794. DOI: http://dx.doi.org/10.1080/02786826.2011.560211.

Nishimura, K, **Nemoto, M.** 2005. Blowing snow at Mizuho Station, Antarctica. *Philosophical Transactions of the Royal Society A: Mathematical, Physical and Engineering Sciences* **363**(1832): 1647–1662. DOI: http://dx.doi.org/10.1098/rsta.2005.1599.

Nishimura, K, **Yokoyama, C**, **Ito, Y**, **Nemoto, M**, **Naaim-Bouvet, F**, **Bellot, H**, **Fujita, K.** 2014. Snow particle speeds in drifting snow. *Journal of Geophysical Research: Atmospheres* **119**(16): 9901–9913. DOI: http://dx.doi.org/10.1002/2014JD021686.

Nixdorf, U, **Dethloff, K**, **Rex, M**, **Shupe, M**, **Sommerfeld, A**, **Perovich, DK**, **Nicolaus, M**, **Heuzé, C**, **Rabe, B**, **Loose, B**, **Ellen, D**, **Rolf, G**, **Allison, F**, **Wieslaw, M**, **Annette, R**, **Ronald, K**, **Gunnar, S**, **Manfred, W**, **Andreas, H**, **Marius, H**, **Verena, M**, **Stephan, F**, **Antonia, I**, **Katharina, W-T**, **Bjela, K**, **Dirk, M**, **Julia, R**, **Peter, G**, **Daniela, R**, **Thomas, K**, **Anne, M**, **Christian, H**, **Torsten, K**, **Frank, RR**, **Vladimir, S**, **Vladimir, S**, **Alexander, M**, **Stefan, S**, **Thomas, W**, **Karsten, W**, **Antje, B.** 2021. MOSAiC extended acknowledgement. Zenodo. DOI: https://doi.org/10.5281/zenodo.5541624.

Norris, SJ, **Brooks, IM**, **de Leeuw, G**, **Smith, MH**, **Moerman, M**, **Lingard, JJN.** 2008. Eddy covariance measurements of sea spray particles over the Atlantic Ocean. *Atmospheric Chemistry and Physics* **8**(3): 555–563. DOI: http://dx.doi.org/10.5194/acp-8-555-2008.

Norris, SJ, **Brooks, IM**, **Hill, MK**, **Brooks, BJ**, **Smith, MH**, **Sproson, DAJ.** 2012. Eddy covariance measurements of the sea spray aerosol flux over the open ocean. *Journal of Geophysical Research: Atmospheres* **117**(D7): D07210. DOI: http://dx.doi.org/10.1029/2011JD016549.

O'Dowd, CD, **Smith, MH**, **Consterdine, IE**, **Lowe, JA.** 1997. Marine aerosol, sea-salt, and the marine sulphur cycle: A short review. *Atmospheric Environment* **31**(1): 73–80. DOI: http://dx.doi.org/10.1016/S1352-2310(96)00106-9.

Overland, J, **Dunlea, E**, **Box, JE**, **Corell, R**, **Forsius, M**, **Kattsov, V**, **Olsen, MS**, **Pawlak, J**, **Reiersen, LO**, **Wang, M.** 2019. The urgency of Arctic change. *Polar Science* **21**: 6–13. DOI: http://dx.doi.org/10.1016/j.polar.2018.11.008.

Peterson, PK, **Hartwig, M**, **May, NW**, **Schwartz, E**, **Rigor, I**, **Ermold, W**, **Steele, M**, **Morison, JH**, **Nghiem, SV**, **Pratt, KA.** 2019. Snowpack measurements suggest role for multi-year sea ice regions in Arctic atmospheric bromine and chlorine chemistry. *Elementa: Science of the Anthropocene* **7**: 14. DOI: http://dx.doi.org/10.1525/elementa.352.

Pithan, F, **Mauritsen, T.** 2014. Arctic amplification dominated by temperature feedbacks in contemporary climate models. *Nature Geoscience* **7**: 181–184. DOI: http://dx.doi.org/10.1038/ngeo2071.

Quinn, PK, **Miller, TL**, **Bates, TS**, **Ogren, JA**, **Andrews, E**, **Shaw, GE.** 2002. A 3-year record of simultaneously measured aerosol chemical and optical properties at Barrow, Alaska. *Journal of Geophysical Research: Atmospheres* **107**(D11): AAC 8-1–AAC 8–15. DOI: http://dx.doi.org/10.1029/2001jd001248.

Rankin, AM, **Auld, V**, **Wolff, EW.** 2000. Frost flowers as a source of fractionated sea salt aerosol in the polar regions. *Geophysical Research Letters* **27**(21): 3469–3472. DOI: http://dx.doi.org/10.1029/2000GL011771.

Rankin, AM, **Wolff, EW.** 2003. A year-long record of size-segregated aerosol composition at Halley, Antarctica. *Journal of Geophysical Research: Atmospheres* **108**(D24): 4775. DOI: http://dx.doi.org/10.1029/2003jd003993.

Rantanen, M, **Karpechko, AY, Lipponen, A, Nordling, K, Hyvärinen, O, Ruosteenoja, K, Vihma, T, Laaksonen, A** 2022. The Arctic has warmed nearly four times faster than the globe since 1979. *Communications Earth & Environment* **3**: 168. DOI: https://doi.org/10.1038/s43247-022-00498-3.

Rayner, NA, **Parker, DE**, **Horton, EB**, **Folland, CK**, **Alexander, LV**, **Rowell, DP**, **Kent, EC**, **Kaplan, A.** 2003. Global analyses of sea surface temperature, sea ice, and night marine air temperature since the late nineteenth century. *Journal of Geophysical Research: Atmospheres* **108**(D14): 4407. DOI: http://dx.doi.org/10.1029/2002jd002670.

Rhodes, RH, **Yang, X**, **Wolff, EW**, **McConnell, JR**, **Frey, MM.** 2017. Sea ice as a source of sea salt aerosol to Greenland ice cores: A model-based study. *Atmospheric Chemistry and Physics* **17**(15): 9417–9433. DOI: http://dx.doi.org/10.5194/acp-17-9417-2017.

Rogers, RR, **Yau, MK.** 1989. *A short course in cloud physics*. Burlington, MA: Butterworth Heinemann.

Roscoe, HK, **Brooks, B**, **Jackson, AV**, **Smith, MH**, **Walker, SJ**, **Obbard, RW**, **Wolff, EW.** 2011. Frost flowers in the laboratory: Growth, characteristics, aerosol, and the underlying sea ice. *Journal of Geophysical Research: Atmospheres* **116**(D12): 301. DOI: http://dx.doi.org/10.1029/2010JD015144.

Saltelli, A, **Annoni, P**, **Azzini, I**, **Campolongo, F**, **Ratto, M**, **Tarantola, S.** 2010. Variance based sensitivity analysis of model output. Design and estimator for the total sensitivity index. *Computer Physics Communications* **182**(2): 259–270. DOI: http://dx.doi.org/10.1016/j.cpc.2009.09.018.

Sander, R, **Keene, WC**, **Pszenny, AAP**, **Arimoto, R**, **Ayers, GP**, **Baboukas, E**, **Cainey, JM**, **Crutzen, PJ**, **Duce, RA**, **Hönninger, G**, **Huebert, BJ**, **Maenhaut, W**, **Mihalopoulos, N**, **Turekian, VC**, **Van Dingenen, R.** 2003. Inorganic bromine in the marine boundary layer: A critical review. *Atmospheric Chemistry and Physics* **3**(5): 1301–1336. DOI: http://dx.doi.org/10.5194/acp-3-1301-2003.

Shupe, MD, **Rex, M**, **Blomquist, BG**, **Persson, PO**, **Schmale, J**, **Uttal, T**, **Althausen, D**, **Angot, H**, **Archer, S**, **Bariteau, L**, **Beck, I**, **Bilberry, J**, **Bucci, S**, **Buck, C**, **Boyer, M**, **Brasseur, Z**, **Brooks, IM**, **Calmer, R**, **Cassano, J**, **Castro, V**, **Chu, D**, **Costa, D**, **Cox, CJ**, **Creamean, J**, **Crewell, S**, **Dahlke, S**, **Damm, E**, **de Boer, G**, **Deckelmann, H**, **Dethloff, K**, **Dütsch, M**, **Ebell, K**, **Ehrlich, A**, **Ellis, J**, **Engelmann, R**, **Fong, AA**, **Frey, MM**, **Gallagher, MR**, **Ganzeveld, L**, **Gradinger, R**, **Graeser, J**, **Greenamyer, V**, **Griesche, H**, **Griffiths, S**, **Hamilton, J**, **Heinemann, G**, **Helmig, D**, **Herber, A**, **Heuzé, C**, **Hofer, J**, **Houchens, T**, **Howard, D**, **Inoue, J**, **Jacobi, H-W**, **Jaiser, R**, **Jokinen, T**, **Jourdan, O**, **Jozef, G**, **King, W**, **Kirchgaessner, A**, **Klingebiel, M**, **Krassovski, M**, **Krumpen, T**, **Lampert, A**, **Landing, W**, **Laurila, T**, **Lawrence, D**, **Lonardi, M**, **Loose, B**, **Lüpkes, C**, **Maahn, M**, **Macke, A**, **Maslowski, W**, **Marsay, C**, **Maturilli, M**, **Mech, M**, **Morris, S**, **Moser, M**, **Nicolaus, M**, **Ortega, P**, **Osborn, J**, **Pätzold, F**, **Perovich, DK**, **Petäjä, T**, **Pilz, C**, **Pirazzini, R**, **Posman, K**, **Powers, H**, **Pratt, KA**, **Preußer, A**, **Quélé ver, L**, **Radenz, M**, **Rabe, B**, **Rinke, A**, **Sachs, T**, **Schulz, A**, **Siebert, H**, **Silva, T**, **Solomon, A**, **Sommerfeld, A**, **Spreen, G**, **Stephens, M**, **Stohl, A**, **Svensson, G**, **Uin, J**, **Viegas, J**, **Voigt, C**, **von der Gathen, P**, **Wehner, B**, **Welker, JM**, **Wendisch, M**, **Werner, M**, **Xie, ZQ**, **Yue, F.** 2022. Overview of the MOSAiC expedition—Atmosphere. *Elementa: Science of the Anthropocene* **10**(1): 00060. DOI: http://dx.doi.org/10.1525/elementa.2021.00060.

Twomey, S. 1977. The influence of pollution on the shortwave albedo of clouds. *Journal of the Atmospheric Sciences* **34**(7): 1149–1152. DOI: http://dx.doi.org/10.1175/1520-0469(1977)034<1149:tiopot>2.0.co;2.

Vetráková, L, **Neděla, V**, **Závacká, K**, **Yang, X**, **Heger, D.** 2023. Technical note: Sublimation of frozen CsCl solutions in an environmental scanning electron microscope (ESEM)—Determining the number and size of salt particles relevant to sea salt aerosols. *Atmospheric Chemistry and Physics* **23**(7): 4463–448. DOI: http://dx.doi.org/10.5194/acp-23-4463-2023.

Wagenbach, D, **Ducroz, F**, **Mulvaney, R**, **Keck, L**, **Minikin, A**, **Legrand, M**, **Hall, JS**, **Wolff, EW.** 1998. Sea-salt aerosol in coastal Antarctic regions. *Journal of Geophysical Research: Atmospheres* **103**(D9): 10961–10974. DOI: http://dx.doi.org/10.1029/97jd01804.

Wagner, DN, **Shupe, MD**, **Cox, C**, **Persson, OG**, **Uttal, T**, **Frey, MM**, **Kirchgaessner, A**, **Schneebeli, M**, **Jaggi, M**, **MacFarlane, AR**, **Itkin, P**, **Arndt, S**, **Hendricks, S**, **Krampe, D**, **Nicolaus, M**, **Ricker, R**, **Regnery, J**, **Kolabutin, N**, **Shimanshuck, E**, **Oggier, M**, **Raphael, I**, **Stroeve, J**, **Lehning, M.** 2022. Snowfall and snow accumulation during the MOSAiC winter and spring seasons. *The Cryosphere* **16**(6): 2373–2402. DOI: http://dx.doi.org/10.5194/tc-16-2373-2022.

Wagner, R, **Kaufmann, J**, **Möhler, O**, **Saathoff, H**, **Schnaiter, M**, **Ullrich, R**, **Leisner, T.** 2018. Heterogeneous ice nucleation ability of NaCl and sea salt aerosol particles at cirrus temperatures. *Journal of Geophysical Research: Atmospheres* **123**(5): 2841–2860. DOI: http://dx.doi.org/10.1002/2017JD027864.

Wolff, EW, **Rankin, AM**, **Röthlisberger, R.** 2003. An ice core indicator of Antarctic sea ice production? *Geophysical Research Letters* **30**(22): 2158. DOI: http://dx.doi.org/10.1029/2003GL018454.

Yang, X, **Blechschmidt, AM**, **Bognar, K**, **McClure-Begley, A**, **Morris, S**, **Petropavlovskikh, I**, **Richter, A**, **Skov, H**, **Strong, K**, **Tarasick, DW**, **Uttal, T**, **Vestenius, M**, **Zhao, X.** 2020. Pan-Arctic surface ozone: Modelling vs. measurements. *Atmospheric Chemistry and Physics* **20**(24): 15937–15967. DOI: http://dx.doi.org/10.5194/acp-20-15937-2020.

Yang, X, **Cox, RA**, **Warwick, NJ**, **Pyle, JA**, **Carver, GD**, **O'Connor, FM**, **Savage, NH.** 2005. Tropospheric bromine chemistry and its impacts on ozone: A model study. *Journal of Geophysical Research: Atmospheres* **110**(D23): 311. DOI: http://dx.doi.org/10.1029/2005JD006244.

Yang, X, **Frey, MM**, **Rhodes, RH**, **Norris, SJ**, **Brooks, IM**, **Anderson, PS**, **Nishimura, K**, **Jones, AE**, **Wolff, EW.** 2019. Sea salt aerosol production via sublimating wind-blown saline snow particles over sea ice: Parameterizations and relevant microphysical mechanisms. *Atmospheric Chemistry and Physics* **19**(13): 8407–8424. DOI: http://dx.doi.org/10.5194/acp-19-8407-2019.

Yang, X, **Neděla, V**, **Runštuk, J**, **Ondrušková, G**, **Krausko, J**, **Vetráková, L**, **Heger, D.** 2017. Evaporating brine from frost flowers with electron microscopy and implications for atmospheric chemistry and sea-salt aerosol formation. *Atmospheric Chemistry and Physics* **17**(10): 6291–6303. DOI: http://dx.doi.org/10.5194/acp-17-6291-2017.

Yang, X, **Pyle, JA**, **Cox, RA.** 2008. Sea salt aerosol production and bromine release: Role of snow on sea ice. *Geophysical Research Letters* **35**(16): 815. DOI: http://dx.doi.org/10.1029/2008GL034536.

Závacká, K, **Neděla, V**, **Olbert, M**, **Tihlaříková, E**, **Vetráková, Ľ**, **Yang, X**, **Heger, D.** 2022. Temperature and concentration affect particle size upon sublimation of saline ice: Implications for sea salt aerosol production in polar regions. *Geophysical Research Letters* **49**(8): e2021GL097098. DOI: http://dx.doi.org/10.1029/2021GL097098.

How to cite this article: Ranjithkumar, A, Duncan, E, Yang, X, Partridge, DG, Lachlan-Cope, T, Gong, X, Nishimura, K, Frey, MM. 2025. Direct observation of Arctic Sea salt aerosol production from blowing snow and modeling over a changing sea ice environment. *Elementa: Science of the Anthropocene* 13(1). DOI: https://doi.org/10.1525/elementa.2024.00006

Domain Editor-in-Chief: Detlev Helmig, Boulder AIR LLC, Boulder, CO, USA

Associate Editor: Hélène Angot, Centre National de la Recherche Scientifique (CNRS), Institute of Environmental Geosciences (IGE), Université Grenoble Alpes, France

Knowledge Domain: Atmospheric Science

Part of an Elementa Special Feature: The Multidisciplinary Drifting Observatory for the Study of Arctic Climate (MOSAiC)

Published: February 04, 2025 **Accepted:** December 02, 2024 **Submitted:** January 26, 2024

ELEMENTA Science of the Anthropocene

Elem Sci Anth is a peer-reviewed open access journal published by University of California Press.

OPEN ACCESS